Joule

CellPress

Article

Concurrent cationic and anionic perovskite defect passivation enables 27.4% perovskite/silicon tandems with suppression of halide segregation

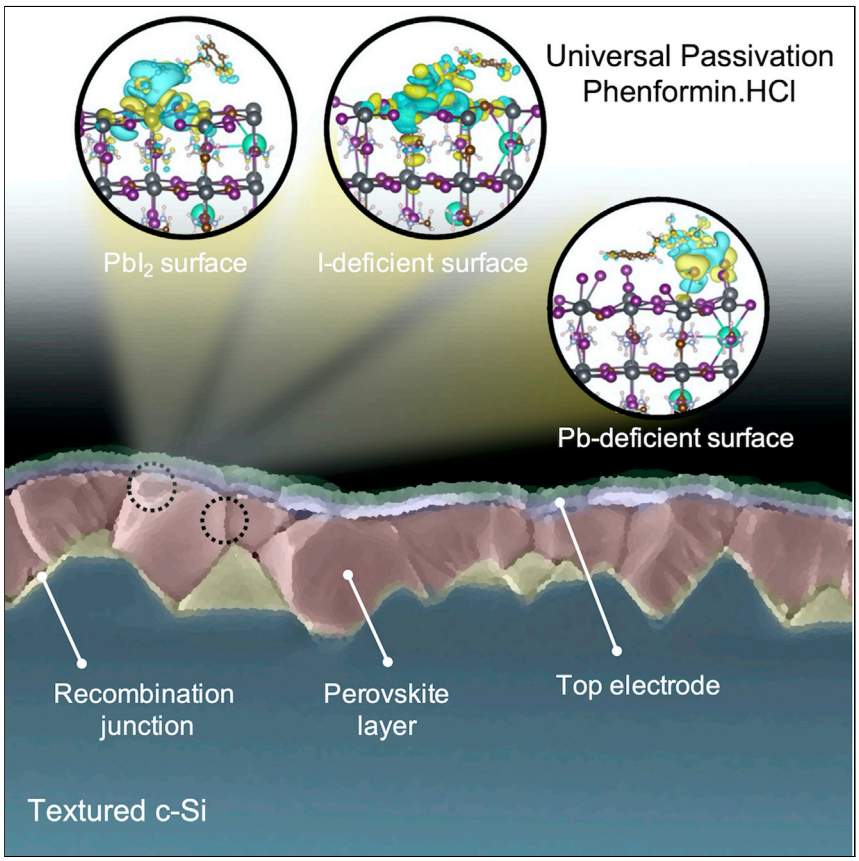

The multi-functional phenformin hydrochloride molecule, incorporating both electron-rich and electron-poor domains, can concurrently passivate cationic and anionic perovskite defects, independent of the perovskite's surface chemical composition and its grain boundaries and interfaces. The concurrent cationic and anionic defect passivation strategy suppresses the light-induced halide segregation issue of the mixed-halide wide-band-gap perovskites, enabling fabrication of high-performance monolithic textured perovskite/silicon tandem solar cells.

Furkan H. Isikgor, Francesco Furlan, Jiang Liu, ..., Udo Schwingenschlögl, Frédéric Laquai, Stefaan De Wolf

furkan.isikgor@kaust.edu.sa (F.H.I.)
stefaan.dewolf@kaust.edu.sa (S.D.W.)

Highlights

Phenformin HCl molecule concurrently passivates cationic and anionic perovskite defects

The concurrent passivation suppresses phase segregation of wide-band-gap perovskites

Phenformin HCl passivation improves the performance of perovskite solar cells

The passivated perovskite/silicon tandem solar cells deliver efficiencies up to 27.4%

Isikgor et al., Joule 5, 1566–1586
June 16, 2021
https://doi.org/10.1016/j.joule.2021.05.013

CellPress

Joule

Article

Concurrent cationic and anionic perovskite defect passivation enables 27.4% perovskite/silicon tandems with suppression of halide segregation

Furkan H. Isikgor,[1,3,*] Francesco Furlan,[1,3] Jiang Liu,[1,3] Esma Ugur,[1] Mathan K. Eswaran,[1] Anand S. Subbiah,[1] Emre Yengel,[1] Michele De Bastiani,[1] George T. Harrison,[1] Shynggys Zhumagali,[1] Calvyn T. Howells,[1] Erkan Aydin,[1] Mingcong Wang,[1] Nicola Gasparini,[1] Thomas G. Allen,[1] Atteq ur Rehman,[1] Emmanuel Van Kerschaver,[1] Derya Baran,[1] Iain McCulloch,[1,2] Thomas D. Anthopoulos,[1] Udo Schwingenschlögl,[1] Frédéric Laquai,[1] and Stefaan De Wolf[1,4,*]

SUMMARY

Stable and efficient perovskite/silicon tandem solar cells require defect passivation and suppression of light-induced phase segregation of the wide-band-gap perovskite. Here, we report how molecules containing both electron-rich and electron-poor moieties, such as phenformin hydrochloride (PhenHCl), can satisfy both requirements, independent of the perovskite's surface chemical composition and its grain boundaries and interfaces. PhenHCl-passivated wide-band-gap (~1.68 eV) perovskite *p-i-n* single-junction solar cells deliver an open-circuit voltage (V_{OC}) ~100 mV higher than control devices, resulting in power conversion efficiencies (PCEs) up to 20.5%. These devices do not show any V_{OC} losses after more than 3,000 h of thermal stress at 85°C in a nitrogen ambient. Moreover, PhenHCl passivation improves the PCE of textured perovskite/silicon tandem solar cells from 25.4% to 27.4%. Our findings provide critical insights for improved passivation of metal halide perovskite surfaces and the fabrication of highly efficient and stable perovskite-based single-junction and tandem solar cells.

INTRODUCTION

Single-junction perovskite solar cells (PSCs) have reached certified power conversion efficiencies (PCEs) of 25.5%, approaching the current record of single-junction silicon solar cells (26.7%), albeit with a smaller active area.[1] The success of PSCs can be ascribed to a high absorption coefficient,[2] a long carrier diffusion length,[3,4] ambipolar charge transport,[5,6] and a high defect tolerance[7,8] of metal halide perovskites. Furthermore, because of their band-gap tunability, perovskites are attractive absorber materials to fabricate multi-junction solar cells aimed at surpassing the single-junction Shockley-Queisser efficiency limit,[9,10] promising high-performance photovoltaics at an affordable cost.[11–15] Specifically, wide-band-gap perovskites (1.65–1.75 eV) made of mixed-halide compositions are critical enablers for efficient silicon-based tandem solar cells as top-cell absorbers. However, extrinsic stressors such as moisture, oxygen, heat, and irradiation alter the perovskite's composition, which might be of concern for commercialization.[16–18] Wide-band-gap perovskites, obtained through partially substituting iodine by bromine in the crystal lattice, are particularly sensitive to such effects,[19,20] leading to segregation into different halide phases under light exposure,[21,22] locally altering the band gap, thereby

Context & scale

Wide-band-gap perovskite solar cells are considered attractive options to build tandem solar cells, combined with well-established silicon bottom cells. However, wide-band-gap perovskites, obtained through partially substituting iodine for bromine in the crystal lattice, suffer from light-induced phase segregation. In addition, perovskites, because of their ionic nature, feature various defect states, which hampers device performance. To address these issues simultaneously, we report a concurrent cationic and anionic perovskite defect passivation strategy using the phenformin hydrochloride molecule, containing both electron-rich and electron-poor functional groups. The concurrent passivation of the perovskite defects suppresses phase segregation of wide-band-gap perovskites and improves performance of monolithic perovskite/silicon tandem solar cells. Consequently, our findings provide critical insights for improved passivation of perovskites and the fabrication of wide-band-gap perovskite-based solar cells.

compromising long-term device stability and robustness.[22] In the case of perovskite/silicon tandems, this also might detrimentally affect current matching conditions. In addition, previous studies have shown a strong correlation between halide segregation and the presence of perovskite surface and grain-boundary defects as well as ion migration.[23,24]

Perovskites, because of their ionic nature, can feature various defect states associated with undercoordinated Pb^{2+} cations, I^-/Br^- anions, organic cation (MA^+/FA^+), and halide vacancies, which tend to accumulate at grain boundaries and perovskite interfaces.[25–27] Such defect states cause charge trapping, non-radiative recombination, and hysteresis, all eroding device performance. Under the influence of extrinsic stressors, defect states can lead to charge accumulation and ion migration, resulting in disruptions in the material lattice. This leads to long-term device instability and performance losses under the PSCs' real-time operation.[28–30]

Defect passivation can reduce non-radiative recombination and enhance device stability, for which various strategies have been proposed recently.[31,32] To passivate bulk defects, various metal cations (e.g., Na^+, Rb^+, K^+, and Cd^{2+}) can be introduced to neutralize undercoordinated I^- ions, interstitials ions, and negatively charged PbI_3^- anti-sites; conversely, anions (e.g., thiocyanate [SCN^-] and acetate [COO^-]) target Pb-interstitial and halide-vacancy neutralization.[33] Certain additives can also control the perovskite film nucleation process, leading to larger gains and thus a reduction in grain boundaries (and their associated trap densities). Functional groups of ionic additives can also aid in defect passivation and the reduction of the mobility of ions in perovskites. Lewis-base additives such as urea, thiophene, poly(methyl methacrylate) (PMMA), and caffeine might donate electrons (from nitrogen, oxygen, and sulfur atoms, respectively) to passivate the undercoordinated Lewis-acid Pb^{2+} cations.[34–38] To passivate I^- defects (PbI_3^- anti-site defects), Lewis-acid molecules such as [6,6]-phenyl-C_{61}-butyric acid methyl ester (PCBM) and zwitterions have been proposed.[39,40] Surface and interface defects might mandate specific passivation strategies. Treating the surface defects with additives such as PMMA, trioctylphosphine oxide (TOPO), and benzylamine is known to suppress phase segregation in wide-band-gap perovskites.[37,41–43] Introducing a thin 2D perovskite layer at the interface can also help to alleviate such defects. Overall, the specific perovskite surface chemistry is crucial in defining adequate passivation strategies. However, most of the early passivation results have been empirical, underlining the need for an improved understanding of the defects involved. Being an ionic mixture of positive and negative charges, the perovskite surface is a strongly susceptive interface, subject to processing details and ambient conditions. Nevertheless, in most cases, the organic and halide species' volatile nature renders the surface lead-rich, featuring undercoordinated Pb^{2+} ions.[44–46] Although larger organic molecules such as phenethylammonium iodide (PEAI), butylammonium iodide (BAI), and other organic ammonium cations are known to form a thin 2D layer and passivate the defects,[47–50] the positively charged molecules cannot effectively passivate the highly positive surface as the Pb^{2+} ions will repel them.

In this work, we aim to design a global passivation strategy that can effectively passivate the perovskite defects both at the grain boundaries and surfaces. For this, a multi-functional passivation molecule that features both electron-rich and electron-poor domains is necessary. Therefore, we propose phenformin hydrochloride (PhenHCl), consisting of electronegative amine and imine groups alongside an electropositive ammonium head group. We find that this molecule effectively passivates the perovskite grain boundaries when incorporated in the perovskite

[1]King Abdullah University of Science and Technology (KAUST), KAUST Solar Center (K.S.C.), Physical Sciences and Engineering Division (PSE), Thuwal 23955-6900, Kingdom of Saudi Arabia

[2]Department of Chemistry, CRL, University of Oxford, Oxford OX13TA, UK

[3]These authors contributed equally

[4]Lead contact

*Correspondence: furkan.isikgor@kaust.edu.sa (F.H.I.), stefaan.dewolf@kaust.edu.sa (S.D.W.)

https://doi.org/10.1016/j.joule.2021.05.013

precursor solution. In addition, it can further alleviate surface defects when employed as a post-treatment molecule. To gain fundamental insights into the passivation mechanisms, we theoretically constructed different perovskite surfaces: a perfectly cleaved lead iodide (PbI_2) surface, an iodide-deficient surface, and a lead-deficient surface. Density functional theory (DFT) calculations demonstrate that the PhenHCl molecule can effectively passivate all of these possible surface-dangling bonds without limitation from the chemical and electronic nature of the surface defects. Because of these enhancements, PhenHCl-passivated single-junction PSCs deliver a ~100 mV higher average V_{OC} than control devices, leading to PCEs above 20% with the best V_{OC} values reaching 1.22 V.

Moreover, steady-state and transient photoluminescence (PL) measurements show that PhenHCl passivation considerably suppresses light-induced phase segregation of wide-band-gap perovskites. PhenHCl passivation also greatly improves the light-soaking and thermal stability of our single-junction devices. The passivated devices show no V_{OC} loss after more than 3,000 h of thermal stress at 85°C in an N_2 environment. Finally, the PhenHCl passivation strategy was employed for the fabrication of perovskite/silicon monolithic tandem solar cells, built onto textured silicon heterojunction solar cells. Here, the passivation improved the average V_{OC} of the tandem devices from ~1.75 to ~1.81 V, and consequently, the average PCE from 23.3% to 26.5%. The best tandem solar cell delivered a V_{OC} of 1.84 V, a short-circuit density (J_{SC}) of 19.6 mA/cm^2, a fill factor (FF) of 76.0%, and a PCE of 27.4%, which is among the highest PCEs reported for monolithic perovskite/silicon tandem solar cells.[51]

We remark that zwitterions, similar to PhenHCl, have electron-rich and -poor functional groups, such as 3-(decyldimethylammonio)-propane-sulfonate inner salt,[52] and were reported to effectively passivate perovskite surface defects. However, unlike most zwitterions, PhenHCl is soluble in perovskite precursor solutions as well as in perovskite-benign solvents, such as isopropanol. Because of this, we elucidate in this study the impact of different PhenHCl passivation strategies (grain boundary passivation, interface passivation, and a combination of both), phase segregation behavior, performance, and stability of PSCs in detail.

RESULTS AND DISCUSSION

DFT calculations

To understand the interaction of $PhenH^+$ with different perovskite surfaces, we performed DFT calculations. Figure 1A shows the chemical structure (top) and electrostatic potential map (bottom) of the $PhenH^+$ molecule. The molecule has various functional groups incorporating electron-rich amine and imine as well as electron-poor ammonium groups. The positive charge on the ammonium head group is counterbalanced by an electronegative chloride anion (Cl^-). Because of the functional groups, the electron cloud surrounding the molecule has electron-rich and electron-poor domains, which are very useful for the passivation of complex perovskite surfaces. To support this, DFT calculations are performed for a supercell with $Cs_{0.13}MA_{0.13}FA_{0.74}Pb(I_{0.81}Br_{0.19})_3$ composition, which is very close to the $Cs_{0.15}MA_{0.15}FA_{0.70}Pb(I_{0.80}Br_{0.20})_3$ composition used in the experimental part of this study. Three different perovskite surfaces are constructed: a perfectly cleaved surface (missing axial I atoms), a highly undercoordinated Pb surface (i.e., a highly I-deficient surface), and a highly undercoordinated I surface (i.e., a highly Pb-deficient surface) as shown in Figures 1B–1D. These surfaces are abbreviated as PbI_2, I-deficient and Pb-deficient surfaces, respectively. The obtained electron density profiles are shown below the surfaces. The profiles highlight that the perovskite

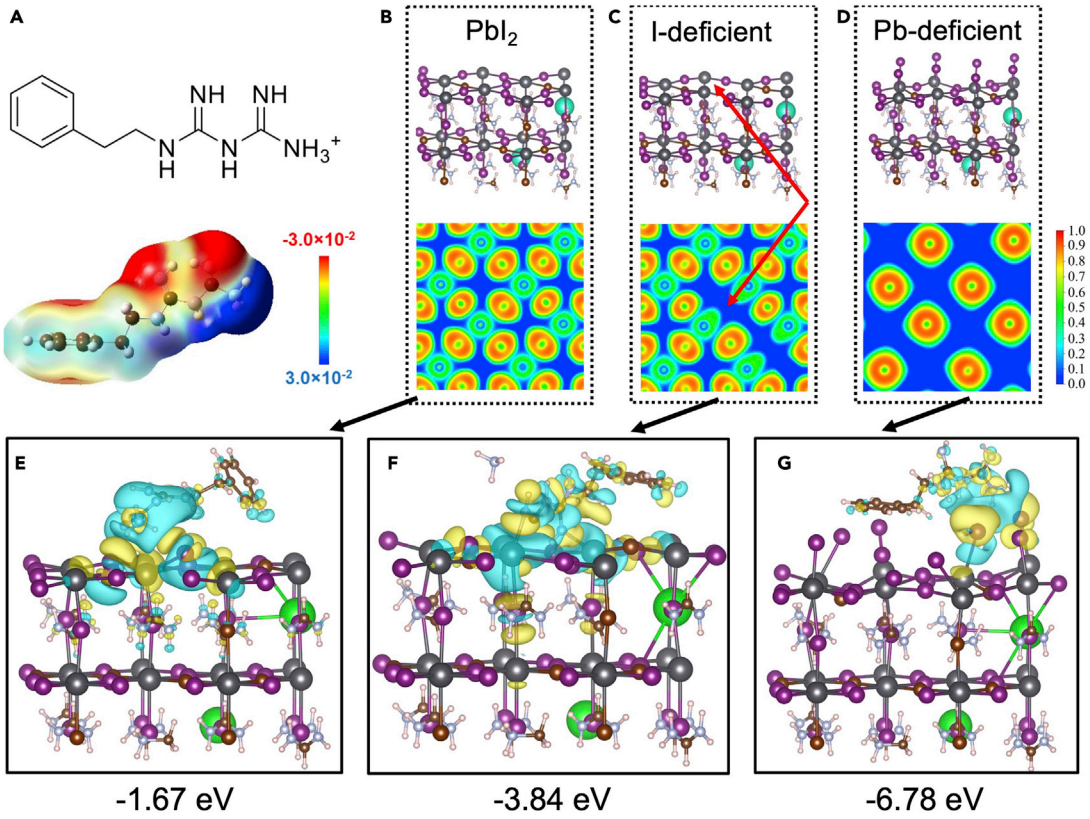

Figure 1. Electrostatic potential maps and binding energies

(A) Chemical structure (top) and electrostatic potential map (bottom) of the $PhenH^+$ molecule.

(B–D) Shown are (B) PbI_2, (C) I-deficient (the I-deficiency is highlighted with the red arrows), and (D) Pb-deficient surfaces studied by DFT, and corresponding top views of the obtained electron density profiles (scale bar on the right).

(E–G) Electron density differences for the $PhenH^+$ molecule on the (E) PbI_2, (F) I-deficient, and (G) Pb-deficient surfaces of $Cs_{0.13}MA_{0.13}FA_{0.74}Pb(I_{0.81}Br_{0.19})_3$, and resultant binding energies. Pink, light brown, light gray, dark brown, violet, green, and gray balls represent the H, C, N, Br, I, Cs, and Pb atoms, respectively.

surfaces consist of a blend of electron-rich and electron-poor domains, the distributions of which are highly influenced by surface defects. Because it is challenging to control the nature of surface defects of metal halide perovskites,[53] multi-functional molecules such as PhenHCl, incorporating electron-rich and electron-poor groups, are expected to be successful for full passivation of the surface defects. Otherwise, a highly electropositive (electronegative) molecule will simply be repelled from an electron-poor (electron-rich) perovskite surface domain because of the unfavorable electrostatic interaction.

Next, we investigate the interaction between the $PhenH^+$ molecule and the three surfaces. The resulting binding energies and Bader charges are summarized in Table S1. The highest binding energy is obtained for the Pb-deficient surface (−6.78 eV), followed by the I-deficient (−3.84 eV) and PbI_2 (−1.67 eV) surfaces. These values are also reflected by the Bader charges, as a positive value indicates that the charge is transferred from the molecule to the surface. Moreover, the electron density difference is calculated to understand the nature of the bonding between the molecule and surface (Figures 1E–1G). The turquoise and yellow regions represent charge depletion and accumulation, respectively. It is clear that $PhenH^+$ can reorient itself depending on the nature of the surface defect and therefore can passivate any

kind of perovskite surface dangling bond. Its electron-deficient NH_3^+ group mostly interacts with the electronegative surface I atoms. In contrast, the electron-rich amine and imine N atoms primarily interact with the electron-poor Pb surface atoms. Interestingly, for the I-deficient surface, the calculations show that the NH_3^+ group detaches from $PhenH^+$. Hence, the amine and imine groups in the molecule interact with the undercoordinated Pb atom, forming the strongest bond. The electron density differences also suggest that one $PhenH^+$ molecule can simultaneously passivate many surface dangling bonds. In addition to this, the counter Cl^- anion of the molecule detaches upon solvation and can passivate undercoordinated Pb surface atoms. The corresponding binding energies for the Cl passivation are given in Table S1. We also present partial densities of states (PDOSs) without and with $PhenH^+$ passivation (Figure S1). For all three non-passivated surfaces (PbI_2, I deficient, and Pb deficient), the valence band edge is mostly due to I states, and the conduction band edge is mostly due to Pb states. Passivation of the PbI_2-terminated surface shifts the Fermi level into the conduction band, passivation of the I-deficient surface results in Pb in-gap states, and passivation of the Pb-deficient surface results in I in-gap states.

We also compare DFT results for $PhenH^+$ and phenethylammonium (PEA^+) passivation, the latter being a commonly used passivation molecule.[54–57] As shown in Figures S2A and S2B, PEA^+, unlike $PhenH^+$, does not exhibit an electron-rich domain on its phenyl alkyl backbone. Although the center of its phenyl ring is electron rich, the ring itself is non-polar, preventing effective passivation of electropositive perovskite surface defects. Binding energy calculations (Table S1) and electron density difference plots (Figures S2C–S2E) show that PEA^+ can passivate the PbI_2 and Pb-deficient surfaces as efficiently as $PhenH^+$. In contrast, in the case of the I-deficient surface, the binding energy (−1.68 eV) is less than half of that in the $PhenH^+$ case. PEA^+ attaches to the I-deficient surface by interaction with the surface I atoms. Because there are fewer I atoms on the I-deficient surface, those atoms tilt to adjust to the PEA^+ molecule, resulting in a highly distorted structure, which might not be advantageous for device stability.[58] In the case where there is no surface I atom close to a Pb-dangling bond, PEA^+ is expected to be repelled from the surface because it lacks electronegative functional groups. The weakness of PEA^+ for passivating the I-deficient surface is also reflected in the calculated PDOS, revealing the existence of in-gap states (Figure S1). These results are highly significant because a hybrid metal halide perovskite surface is expected to have a more I-deficient character if no post-treatment is applied.[44] The reason is that volatile halide species are expected to outgas preferentially from the surface (in the form of HX or X_2; X: I and/or Br) during the annealing process.[45,46] Hence, we speculate that multi-functional molecules such as PhenHCl, which incorporate both electron-rich and electron-poor functional groups, are more effective for passivation of metal halide perovskite-dangling bonds than commonly used organic ammonium salts (such as PEA^+, butylammonium, allylammonium, and benzylammonium halides) missing electron-rich functional groups.

PhenHCl-passivated *p-i-n* single-junction wide-band-gap PSCs

Scheme 1 shows a schematic of the device structure, which has the following *p-i-n* architecture: indium tin oxide (ITO)/poly(triaryl)amine (PTAA)/perovskite/C_{60}/bathocuproine (BCP)/Ag. Before spin casting the perovskite precursor solution, the PTAA surface is treated with a cesium iodide (CsI) solution to form artificial nucleation sites and consequently improve the wettability of the PTAA surface (further details in Figures S3 and S4 and Note S1). As depicted, the PhenHCl molecule is employed to enable grain boundary passivation (GBP) and top surface passivation (TSP) of the perovskite. As the wide-band-gap perovskite, we choose $Cs_{0.15}MA_{0.15}FA_{0.70}PbI_{(0.80}Br_{0.20)3}$ because of its ideal band gap (~1.68 eV) for the fabrication of perovskite/silicon tandem solar cells.[11,15] To

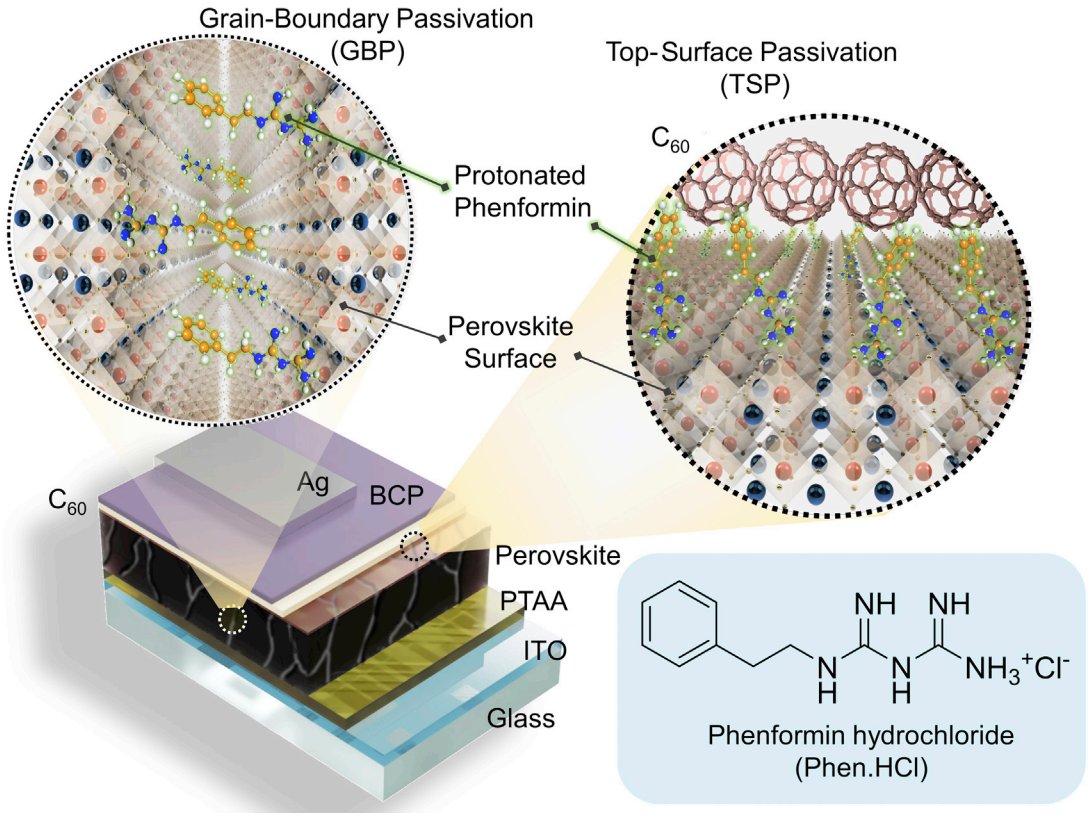

Scheme 1. Illustration of the *p-i-n* device structure, GBP and TSP strategies, and the molecular structure of the PhenHCl passivation molecule used in this study

passivate the perovskite grain boundaries, specific concentrations of PhenHCl are added into the perovskite precursor solutions. As shown in Figure S5, the average V_{OC} of the control devices improves from 1.08 to 1.16 V when the concentration of PhenHCl in the perovskite solution reaches 1 mg/mL. From a device perspective, the optimum PhenHCl concentration for GBP is 0.25 mg/mL, resulting in an average V_{OC} of 1.15 V. We find that when the PhenHCl concentration exceeds 0.25 mg/mL, the FF of the devices decreases (Figure S5D). For the TSP case, specific concentrations of PhenHCl, dissolved in isopropanol, are spin coated onto the perovskite thin film to passivate its top surface (i.e., the perovskite-C_{60} interface, Scheme 1), followed by annealing at 100°C for 5 min. Although the V_{OC} of the control devices improves with increasing PhenHCl concentration, again, the FF values start to drop for concentrations higher than 0.5 mg/mL (Figure S6). Consequently, 0.75 mg/mL PhenHCl is found to be the optimum concentration for TSP. After further process optimization, annealing of the PhenHCl-coated perovskite layer at 80°C for 5 min was found to deliver the best performance (Figure S7).

Figures 2A–2D summarizes the main photovoltaic parameters for the performance for PSCs fabricated with GBP, TSP, a combination of both (GBP+TSP), and control devices. Notably, all passivation routes improve the V_{OC} without resulting in a FF drop for the optimized PhenHCl concentrations. The average V_{OC} of the control devices increases from 1.08 to 1.15, 1.11, and 1.18 V for the GBP, TSP, and GBP+TSP, respectively (Figures 2A and 2B). All devices reach J_{SC} values slightly above 21 mA/cm^2, close to the integrated J_{SC} of 20.5 mA/cm^2 obtained from the external quantum efficiency (EQE) spectra (Figure S8A). The EQE spectra do not change

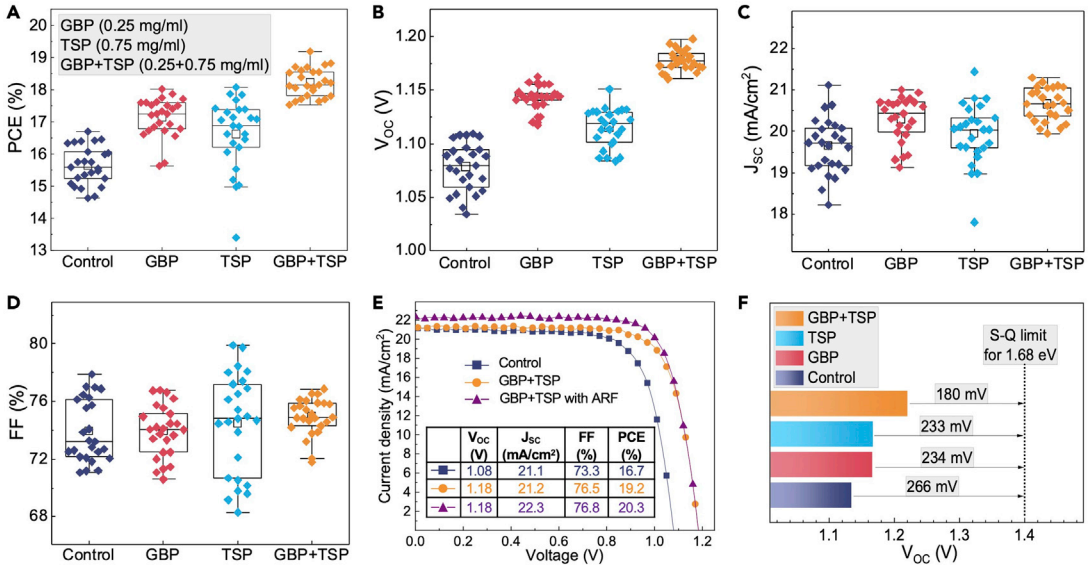

Figure 2. Single-junction device efficiencies

(A–D) Shown are (A) PCE, (B) V_{OC}, (C) J_{SC}, and (D) FF statistics of the control $Cs_{0.15}MA_{0.15}FA_{0.70}Pb(I_{0.80}Br_{0.20})_3$ PSCs with PTAA as HTL in comparison to GBP, TSP, and GBP+TSP conditions.

(E) *J-V* curves of the best-performing control $Cs_{0.15}MA_{0.15}FA_{0.70}Pb(I_{0.80}Br_{0.20})_3$ PSC with PTAA as HTL compared with GBP+TSP and GBP+TSP with a PDMS ARF. The inset table shows the corresponding *J-V* parameters.

(F) Graph showing maximum achievable V_{OC} of PSCs with 2PACz as hole-selective contact, and V_{OC} losses of each condition for the Shockley-Queisser limit of a single-junction solar cell (1.40 V) with a band gap of 1.68 eV at 25°C.

considerably upon passivation. The control and passivated perovskites have similar band gaps (~1.68 eV, extracted from the first derivative of the EQE curves [*d*EQE/*d*λ, Figure S8B]). On the other hand, the passivation treatments cause a slight increase in average series resistance (R_s) from 3.5 to 3.8–4.5 Ω cm^2 (Figure S9A). The increase in R_S is counterbalanced by an increase in the average shunt resistance (R_{sh}) from 2.5 to 5.0–6.1 kΩ cm^2 (Figure S9B). Consequently, the passivation procedures do not have a considerable effect on the FF. A comparison of the *J-V* curves of the best-performing control (with a PCE of 16.7%, a V_{OC} of 1.08 V, a FF of 73.3%, and a J_{SC} of 21.1 mA/cm^2) and GBP+TSP devices is shown in Figure 2E. The V_{OC} of the champion GBP+TSP device shows an improvement of 100 mV, reaching 1.18 V and a PCE of 19.2%. When a polydimethylsiloxane (PDMS) anti-reflective foil (ARF) is applied on the glass side, the J_{SC} improves by about 1 mA/cm^2 due to reduced reflectance, resulting in a champion cell PCE of 20.3%. We also fabricated *p-i-n* devices with [2-(9H-carbazol-9-yl)ethyl]phosphonic acid (2PACz) self-assembled monolayer (SAM) as the hole-selective contact (Figure S10). Similar to the PTAA case, the 2PACz-based devices perform better when a combination of GBP and TSP is used. The champion device delivers a V_{OC} of 1.22 V with a PCE of 20.5% (with ARF). The 2PACz-based devices deliver slightly higher V_{OC} values than PTAA because the SAM-modified ITO surface has a higher work function (WF, 5.0 eV) than PTAA (4.3 eV).[59] These are among the highest efficiencies reported in the literature for such wide-band-gap perovskites, designed for implementation in perovskite/silicon tandem solar cells.[51] Figure 2F compares the minimal achievable V_{OC} losses obtained for each Shockley-Queisser limit condition for single-junction solar cells at 25°C.[60] As shown, for the devices incorporating 2PACz as hole-selective contact, a combination of GBP and TSP decreases the V_{OC} loss from 266 to 180 mV. This loss can be further minimized by implementing interlayer materials with improved energy alignment with respect to the perovskite absorbers.[61]

To verify the concurrent cationic and anionic defect passivation capabilities of PhenHCl, we fabricated PSCs with I-deficient (PbI_2-rich) and Pb-deficient (MAI-rich) surfaces. Experimental details for the fabrication of these PSCs are provided in the supplemental information. Briefly, the perovskite films are overannealed to trigger outgassing of the volatile organic and halide components and consequently to obtain an I-deficient surface with undercoordinated Pb^{2+} ions.[44] Conversely, other films are dipped into an MAI solution (5 mg/mL in IPA) to enable diffusion of the excess MA^+ and I^- ions into the film,[62] and consequently to obtain a Pb-deficient surface. X-ray diffraction (XRD) patterns of these post-treated films (Figure S11) show the existence of excess PbI_2 (~12.8°) and MAI (~9.7° and ~19.7°) peaks,[63,64] proving formation of the I-deficient and Pb-deficient perovskite surfaces, respectively. Figure S12 shows photovoltaic parameters for the performance of PSCs with such post-modified surfaces. As shown, when the optimized TSP approach is employed, the average V_{OC} of the PSCs with the I-deficient surface improves from 1.08 to 1.13 V. Consequently, the average PCE of the devices increases from 15.6% to 17.2%. A similar trend is observed for the devices having Pb-deficient surfaces, too. These results further support that multi-functional PhenHCl molecule can effectively passivate perovskite surfaces having different chemical compositions and ionic natures.

Further, the hysteresis of the devices is investigated by analyzing their forward (−0.1 → 1.2 V) and reverse (1.2 → −0.1 V) scan *J-V* curves (Figure S13). The control devices have a low average hysteresis index (defined as $1-[PCE_{forward}/PCE_{reverse}]$) of $\sim 3.5 \times 10^{-2}$. The passivation procedures reduce the average hysteresis index even further to $\sim 1.5 \times 10^{-2}$, $\sim 1.9 \times 10^{-2}$, and $\sim 1.8 \times 10^{-2}$ for the GBP, TSP, and GBP+TSP cases, respectively. Because ion migration has been proposed as a cause of photovoltaic *J-V* hysteresis in hybrid PSCs,[65] reduction of the hysteresis can be correlated to increased suppression of ion migration upon passivation. In this respect, PhenHCl can effectively passivate the dangling bonds on the perovskite surface and reduce surface-induced ion migration.

To verify the potential of PhenHCl passivation, we comparatively studied the performance of the *p-i-n* PSCs passivated with PEAI. Details of PEAI passivation are discussed in Note S2. Figure S14 compares wide-band-gap PSCs passivated with PhenHCl and PEAI molecules. Here, we note that a GBP+TSP combination is employed for both passivation agents. The devices are fabricated and measured under identical conditions. The PSCs passivated with PEAI have slightly higher FF values; average FF values are 75.7% and 74.5%, respectively, for the PEAI- and PhenHCl-passivated devices. On the other hand, the PhenHCl passivation delivers a significantly higher V_{OC}. The PhenHCl-passivated devices have an average V_{OC} of 1.18 V, compared with 1.14 V for the PEAI case. Similarly, the best V_{OC} values are 1.20 V and 1.17 V, respectively. These results show that PhenHCl passivation produces about a 30–40 mV higher V_{OC} than PEAI passivation. This can be explained by the multi-functional groups existing on the PhenHCl molecule, particularly electron-rich amine and imine nitrogens, absent on PEAI.

Stability of single-junction *p-i-n* wide-band-gap PSCs

We also investigated the impact of both PhenHCl and PEAI passivation on device stability. Figure 3A shows the maximum power point (MPP) evolution tracked under 1-sun illumination over 600 s. The corresponding MPP voltage (V_{MPP}) and current density (J_{MPP}) tracks are given in Figure S15. Interestingly, the control device's PCE rapidly drops by about 0.6% absolute (from 17.3% to 16.7%, indicated with the red square) during the first minute of MPP tracking, whereas the passivated

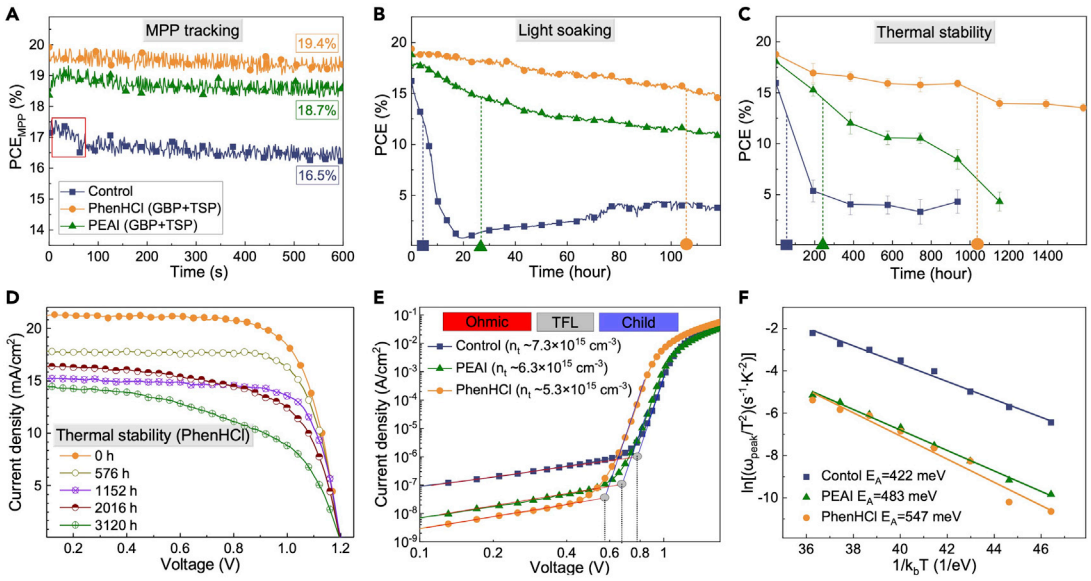

Figure 3. Single-junction device stabilities and density of trap states

(A–C) Shown are (A) MPP tracking, (B) light-soaking stability, and (C) thermal stability of the control (dark blue square), PEAI- (green triangle), and PhenHCl-passivated (orange circle) devices. The thermal stability PCE curves were obtained from an average of four devices for each of the conditions.

(D) *J-V* curves of a PhenHCl-passivated PSC were taken at different time durations under the thermal stability test at 85°C without encapsulation in an N_2-filled glove box.

(E) SCLC measurement in the dark showing the *J*−*V* traces with three different regimes of operation for the control (dark blue square), PEAI- (green triangle), and PhenHCl-passivated (orange circle) devices.

(F) Arrhenius plots of $\ln(\omega_{peak}/T^2)$ as a function of the temperature using the trap peak frequencies (ω_{peak}) of the control, PEAI-passivated, and PhenHCl-passivated devices with the extracted activation energies.

devices exhibit a more stable power output. We attribute the initial PCE drop of the control devices to photo-induced phase segregation of the mixed-halide perovskite.[22] To investigate this further, we tested the stability of the devices under continuous light soaking, without encapsulation under N_2 flow. The symbols projected on the x axis show the average T80 lifetimes (the time required to reach 80% of initial performance) of the devices. As shown in Figure 3B, the control device degrades 20% in relation to its initial PCE in less than 5 h (dark blue square). The PEAI-passivated device exhibits an improved photostability compared with the control device as it takes ~27 h (green triangle) to lose 20% of its initial PCE. On the other hand, the PhenHCl-passivated device exhibits the best photostability as it retains 80% of its post-burn-in PCE for ~106 h (orange circle) of operation. The thermal stability of the devices is also tested by heating the devices at 85°C without encapsulation in an N_2-filled glove box (Figure 3C). For this, the average PCE values of four devices for each condition were recorded every ~8 days (~192 h). In line with these light-soaking tests, the PhenHCl-passivated devices exhibit outstanding thermal stabilities by retaining 80% of their average PCE after more than 1,000 h. In contrast, the PEAI-passivated and control devices retain 80% of their average PCE only for ~240 and ~50 h, respectively. Figure 3D shows the *J-V* curves of a PhenHCl-passivated PSC taken at different time durations under the thermal stability test at 85°C. As shown, the PCE loss is mainly due to the reduction in J_{SC}; however, no loss is observed in the V_{OC} after more than ~3,100 h of the thermal stability test, underlining the outstanding stability of the PhenHCl passivation. Figures S16 and S17 show the evolution of V_{OC}, J_{SC}, and FF values of the control, PEAI-passivated, and PhenHCl-passivated devices under light-soaking and thermal stability tests. For the control device, all of the efficiency parameters drop rapidly. On the other

hand, a steady loss in J_{SC} values is the main culprit behind the efficiency losses of the PEAI- and PhenHCl-passivated devices. Interestingly, the FF and V_{OC} of the PEAI-passivated device are stable under continuous light illumination, which is not the case for the thermal stability test. These results suggest that the degradation behavior of PSCs passivated with different molecules can show different trends depending on the nature of the stability test. Hence, further investigations are required to understand the degradation mechanisms of the control and passivated PSCs under different stability test conditions.

To extract the density of trap states (n_t) and further understand the passivation effect on the device stabilities, we conducted space-charge limited current (SCLC) measurements (Figure 3E). From the trap-filled limit voltage (V_{TFL}) of the devices, n_t values are calculated to be 7.3×10^{15} cm^{-3}, 6.3×10^{15} cm^{-3}, and 5.3×10^{15} cm^{-3} for the control, PEAI- and PhenHCl-passivated devices, respectively. The low trap density can explain the better operational stabilities of PhenHCl-passivated devices as trapped charges play a decisive role in the irreversible degradation of metal halide perovskites. In this respect, Ahn et al.[19] also reported that the beginning of irreversible decomposition could be attributed to local electric fields induced by trapped charges. They demonstrated that perovskites degrade irreversibly along surfaces (grain boundaries and interfaces) only when both moisture and trapped charges exist simultaneously, regardless of the charge polarity.

In addition, and as already stated above, another route of degradation is the compositional instability of wide-band-gap mixed-halide (I and Br) perovskites under illumination. In principle, passivation of trap states should limit halide ion migration in these regions and consequently suppress phase segregation.[66,67] Thus, we also extracted the activation energy (E_A) for ion diffusion in control and passivated samples by using thermal admittance spectroscopy. Activation energies of the ionic conductivity are calculated from the frequencies (ω) of the $-\omega dC/d\omega$ spectra peaks in the low-frequency region for the temperature interval of 250–320 K (Figures 3F and S18). The results show that PhenHCl passivation increases the E_A required for ion diffusion from 422 to 547 meV, higher than PEAI (483 meV). These findings suggest that PhenHCl is highly effective in suppressing halide segregation, reflected in significantly improved device stabilities.

Spectroscopic characterization

To investigate the passivation effect on the charge carrier recombination dynamics of the wide-band-gap perovskite films, we measured time-resolved photoluminescence (TRPL) of the control and passivated films. Figure 4A shows the 2D pseudo-color PL emissions from the control and PhenHCl-passivated (GBP+TSP) samples (results from the GBP and TSP samples are given in Figure S19). The highest PL intensity and longest carrier lifetime are obtained when a combination of GBP and TSP is employed, which is also evident from absolute PL imaging of the samples (Figure 4B), acquired by using hyperspectral microscopy. The entire PL spectrum fit is based on Würfel's generalized Planck law and the absorptivity extracted from the PL spectra.[68–70] As shown, the control sample features lower band-gap emission than the passivated sample, which gives evidence of phase segregation in the control sample, highlighting the existence of minority iodide-rich and majority bromide-rich domains.[22] Although the iodide-rich domains have low volume fractions, they dominate the PL emission because photo-generated carriers relax into lower energy states. Hence, emission occurs from the lowest band-gap domains. Absolute PL imaging of the PhenHCl-passivated sample indicates that PhenHCl passivation effectively suppresses phase segregation. Figure 4C shows band-gap imaging of the

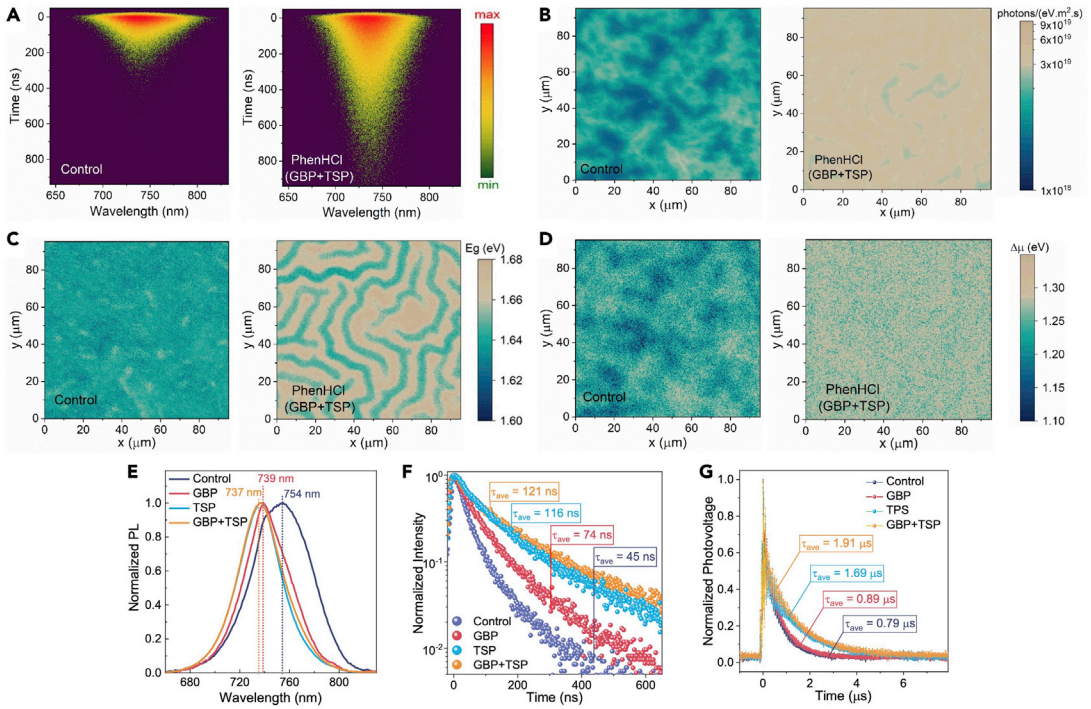

Figure 4. Comparison of control and PhenHCl-passivated (GBP+TSP) wide-band-gap perovskite thin films

(A–D) Shown are (A) 2D pseudo-color streak camera, (B) absolute PL intensity, (C) band-gap, and (D) QFLS images. For both TRPL and absolute PL measurements, the films are excited at 532 nm from the surface of the perovskite.

(E–G) Shown are (E) Normalized steady-state PL spectra, (F) TRPL kinetics, and (G) TPV of control wide-band-gap perovskites compared with PhenHCl-passivated samples with GBP, TSP, and GBP+TSP.

control and PhenHCl-passivated samples. In line with the absolute PL imaging results, PhenHCl passivation is found to suppress the formation of lower band-gap states on a large scale. We use the same intensity scale (in log scale) for the control and passivated samples to make the PL images comparable. To make a better comparison, we show the PL intensity and Eg images of the passivated perovskite sample in Figure S20. Figure 4D also confirms that the passivation uniformly increases the quasi-Fermi level splitting (QFLS), giving further evidence that PhenHCl passivation effectively reduces non-radiative recombination losses. Figure 4E compares the normalized steady-state PL spectra; the non-normalized PL spectra are given in Figure S21A. The TSP and GBP+TSP thin films show the characteristic PL peak at around 738 nm, corresponding to a band gap of ~1.68 eV. On the other hand, the maximum PL intensity of the control and GBP samples red shifts to 754 and 739 nm, respectively (Figures S21B and S21C). In addition, the main PL peaks of these samples can be deconvoluted into two peaks having maximum emissions at around 740 and 760 nm, respectively. These observations suggest that the control and GBP thin films exhibit two different perovskite phases under light illumination. Although the GBP process effectively reduces the full width half maximum of the PL spectrum of the control sample from ~57 to ~43 nm, the deconvoluted PL signal indicates the existence of a secondary perovskite phase, emitting at ~760 nm, which is reduced compared with the control sample. Hence, TSP or a GBP+TSP combination is required to suppress the formation of these phases (Figures S21D and S21E), highlighting the importance of passivation of the perovskite top surface, which is here the perovskite/C_{60} interface. Furthermore, in line with the absolute PL measurements, the time-resolved PL (TRPL) decays indicate that PhenHCl passivation incrementally

enhances the PL lifetime from 45 to 121 ns following GBP and TSP (Figure 4F). Therefore, reducing the non-radiative recombination losses leads to a V_{OC} enhancement of ~100 mV on average device level (Figure 2B). In line with the TRPL results, transient photovoltage decay (TPV) curves of the complete devices also show an increasing trend from 0.79 to 1.91 μs when using PhenHCl passivation (GBP+TSP) (Figure 4G).

Our findings suggest that GBP reduces halide segregation in the perovskite (Figures 4E and S21), yet additional surface passivation is essential to overcome this issue entirely. The enhancement in steady-state PL intensities and TRPL lifetimes indicates that PhenHCl passivation of the perovskite surface reduces the halide segregation because of a reduced number of surface defects. In line with our findings, Belisle et al.[23] also reported that perovskite surfaces are an integral part of the halide segregation process; charge accumulation and carrier trapping at perovskite surfaces are principal drivers of photo-induced halide segregation. Hence, effective passivation of dangling bonds at the perovskite's surfaces is a pathway to achieve phase stabilization of wide-band-gap perovskites. Moreover, PhenHCl passivation increases the activation energy (Figure 3F) required for ion diffusion by ~125 meV compared with the control sample. This restricts ion diffusion in the wide-band-gap perovskite film and thus suppresses phase segregation.[24] Furthermore, employing excess halide reduces the density of halide vacancies, which is the main reason for halide migration and segregation.[71] Thus, we believe that additional Cl^- ions from the PhenHCl salt could also help minimize the density of halide vacancies and suppress phase segregation.[72]

Thin film characterization

Ultraviolet photoelectron spectroscopy (UPS) was used to acquire the energetic dependence of PhenHCl passivation on the perovskite film. As shown in Figure 5A, we observe a concomitant decrease in the WF (determined from the secondary electron cutoff) for TSP and GBP+TSP. In contrast, the GBP alone does not have a significant impact on the WF. Compared with the control samples, PhenHCl passivation results in the formation of deeper valence band maximum (VBM) levels (Figure 5B). Figure 5C represents the energetic positions of ITO, PTAA, C_{60}, and pristine and passivated perovskite (GBP, TSP, and GBP+TSP). The schematic shows that the PhenHCl-passivated (GBP+TSP) sample has a band offset of 0.38 and 0.24 eV, respectively, with PTAA and C_{60}. Further, X-ray photoelectron spectroscopy (XPS) was used to analyze the presence of PhenHCl in the passivated samples. Shown in Figures 5D and 5E are the C1s and N1s spectra of the pristine (top) and PhenHCl-passivated (GBP+TSP, bottom) samples, respectively. The peak assignments are fully detailed in the supplemental information (Figures S22–S26 and Note S3). The N1s and C1s line shapes of the control and passivated films differ significantly. The N1s and C1s surveys of the passivated sample can be understood as a linear combination of the $PhenH^+$ and perovskite peaks. Also, Pb4f XPS survey scans of the control and TSP $Cs_{0.15}MA_{0.15}FA_{0.70}Pb(I_{0.80}Br_{0.20})_3$ perovskites are collected with a photoemission take-off angle of 63°, to reduce XPS sampling depth to 4–5 nm.[73] As shown in Figure S27, the Pb4f peaks of the control sample shift to lower binding energy by ~0.5 eV after the TSP. In line with previously reported studies,[38] this shows that surface Pb atoms of the perovskite become more electron rich when the electron-rich nitrogen atoms of PhenHCl bind to the undercoordinated Pb surface atoms. Figures 5F and S28 show top-surface scanning electron microscopy (SEM) images of the control and PhenHCl-passivated films. The SEM images indicate that the passivation does not have a considerable impact on the grain size. Hence, the observed V_{OC} enhancements are indeed due to the passivation of surface

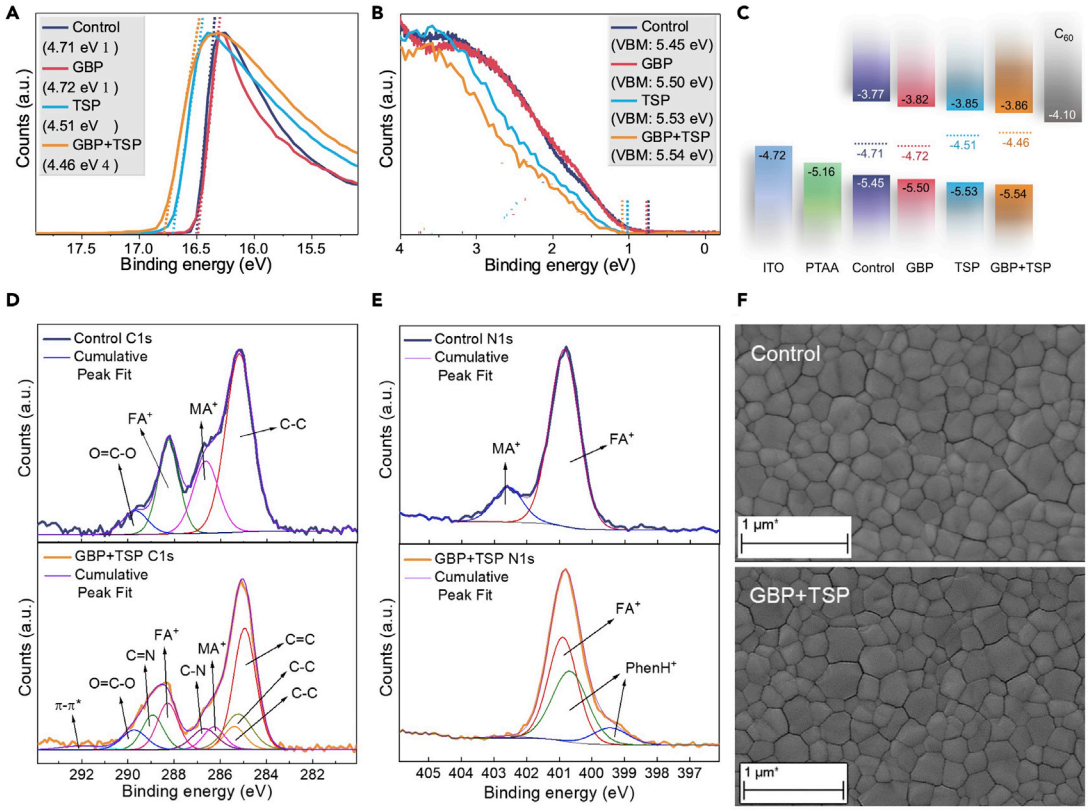

Figure 5. Thin-film characterizations

(A) UPS (He(I) 21.22 eV) spectra of the control and PhenHCl-passivated $Cs_{0.15}MA_{0.15}FA_{0.70}Pb(I_{0.80}Br_{0.20})_3$ perovskite thin films. Secondary electron cutoff (SECO) from which the WF is extracted.

(B) Valence band edge region intensity on a linear scale of the control and PhenHCl-passivated $Cs_{0.15}MA_{0.15}FA_{0.70}Pb(I_{0.80}Br_{0.20})_3$ perovskite thin films. The vertical lines identify the estimated VBM onsets.

(C) Conduction band minimum (CBM), VBM, and WF values of ITO, PTAA, C_{60}, pristine perovskite thin film, and PhenHCl-passivated perovskite thin films.

(D and E) XPS (Al Kα 1,486.6 eV) spectra are showing high-resolution (D) C1s and (E) N1s surveys of the control (top) and PhenHCl-passivated (GBP+TSP, bottom) perovskite films.

(F) Top SEM images of the control (top) and PhenHCl-passivated (GBP+TSP, bottom) perovskite films.

dangling bonds but not due to the improved crystallinity and grain size of the perovskite layer. XRD and absorptance spectra of the pristine and passivated samples further confirm this as both samples exhibit the same patterns (Figures S29 and S30). In addition, the XRD spectra of the passivated samples do not exhibit low reflection peaks, implying that PhenHCl passivation does not form a 2D perovskite layer. Atomic force microscopy (AFM) height images reveal that the root-mean-square roughness (R_{RMS}) of the control sample (18.5 nm) slightly increases to ~28 and ~24 nm after the GBP and TSP processes, respectively (Figure S31).

Perovskite/silicon textured tandem solar cells

Next, we integrated the 1.68 eV wide-band-gap $Cs_{0.15}MA_{0.15}FA_{0.70}Pb(I_{0.80}Br_{0.20})_3$ perovskite on top of a silicon heterojunction (SHJ) bottom cell to fabricate perovskite/silicon tandem solar cells. *J-V* curves of the SHJ cell measured under 1- and 0.5-sun illuminations are given in Figure S32. In light of the recent advances in the tandem field,[74] here we employed 2PACz SAM as the hole-selective contact of the perovskite layer for fabrication of the perovskite layer. Figure 6A gives the device sketch and corresponding cross-sectional SEM image. Here, a perovskite solution

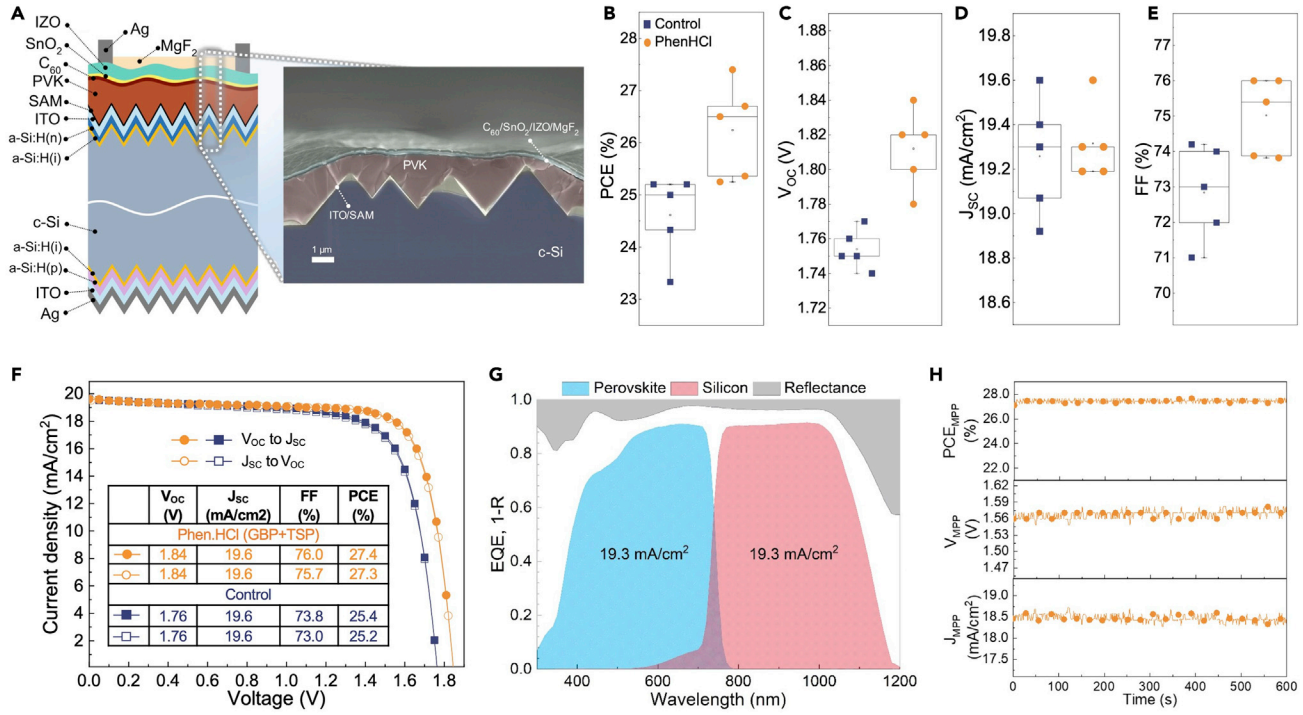

Figure 6. Monolithic perovskite/silicon tandem solar cell efficiencies

(A) Schematic of solution-processed perovskite/silicon tandem solar cell architecture, built onto a textured SHJ solar cell. a-Si:H(n), n-doped hydrogenated amorphous silicon; a-Si:H(i), intrinsic hydrogenated amorphous silicon; a-Si:H(p), p-doped hydrogenated amorphous silicon; SAM, 2PACz; PVK, perovskite. The cross-sectional SEM image highlights the textured SHJ surface, the recombination junction, and the top perovskite sub-cell.

(B–E) Shown are (B) PCE, (C) V_{OC}, (D) J_{SC}, and (E) FF statistics of the control and PhenHCl-passivated (GBP+TSP) tandem solar cells.

(F) *J-V* curves of the best-performing control and PhenHCl-passivated perovskite/textured SHJ tandem solar cells. The inset table shows the corresponding efficiency parameters.

(G) Corresponding EQE of the champion perovskite/SHJ monolithic tandem cells. The gray shaded area in the EQE graph shows the 1-R data.

(H) MPP tracking measurement of the champion PhenHCl-passivated perovskite/textured SHJ tandem solar cell with PCE_{MPP} (top), V_{MPP} (middle), and J_{MPP} (bottom) values for 10 min.

processing technique reported by Hou et al.[15] is employed to fully cover the textured silicon surface with a micrometer-thick perovskite layer. Figures 6B–6E compare the efficiency parameters of the control and PhenHCl-passivated (GBP+TSP) tandem solar cells. In line with the single-junction device results, PhenHCl passivation particularly improves the average V_{OC} of the tandem devices by ~60 mV in addition to an average ~3% absolute improvement in the FF. The best V_{OC} of the passivated devices reaches 1.84 V. The enhancements in V_{OC} and FF can be attributed to reduced recombination losses at the perovskite grain boundaries and top surface after passivating the dangling perovskite surface bonds with PhenHCl. Nevertheless, the high V_{OC} enhancement (~100 mV, Figure S10) of the SAM incorporating PhenHCl-passivated single-junction devices is not fully reflected in the tandem devices. We attribute this to a possible coverage issue of the SAM on the textured Si surface, particularly on the pyramid tips. As such, the average R_{sh} of the single-junction devices is ~6.1 kΩ cm^2, whereas it drops to ~1.7 kΩ cm^2 for the case of tandem devices. This suggests that the tandem devices have a slightly higher shunt, reducing the V_{OC} of the devices. Even so, mainly due to the V_{OC} enhancement by passivation, the average PCE of the tandem devices increases from 23.3% to 26.5%. As shown in Figure 6F, the passivated devices deliver the highest PCE of 27.4%, whereas the best PCE of the control device remains at 25.4%. The EQE of

the best PhenHCl-passivated tandem device (Figure 6G) shows that the sub-cells are current matched at 19.3 mA/cm^2, being very close to the J_{SC} of 19.6 mA/cm^2 measured from the *J-V* curve. MPP tracking of the passivated tandem device over 10 min demonstrates a stabilized PCE of 27.4% (Figure 6H).

Conclusion

In this study, we demonstrate that multi-functional compounds such as PhenHCl, incorporating both electron-rich and electron-poor domains, can effectively passivate perovskite surface dangling bonds and suppress phase segregation without being limited by the electronic and compositional nature of the surface. We have shown that such multi-functional compounds lead to improved passivation of perovskites than commonly reported organic mono-cationic passivation compounds such as PEAI. Taking these advantages, we found that PhenHCl-passivated devices deliver ~100 and ~40 mV higher V_{OC} than control and PEAI-passivated devices, respectively. In addition, PhenHCl passivation considerably improves the operational and thermal stabilities of wide-band-gap PSCs by effectively reducing ion migration and consequently phase segregation. Finally, PCEs reaching 27.4% were obtained when the PhenHCl passivation is employed to fabricate perovskite/silicon monolithic tandem solar cells. This is among the highest PCEs reported for monolithic perovskite/silicon tandem devices.[51] Hence, a better understanding of perovskite surface passivation with multi-functional compounds can potentially further push the current PCEs toward the Shockley-Queisser limit.

EXPERIMENTAL PROCEDURES

Resource availability

Lead contact

Further information and requests for resources should be directed to and will be fulfilled by the lead contact, Stefaan De Wolf (stefaan.dewolf@kaust.edu.sa).

Materials availability

This study did not generate new unique materials.

Data and code availability

The published article and its supplemental information include all data generated or analyzed during this study.

Materials

Patterned ITO glass substrates (15 Ω □$^{-1}$) were obtained from Xinyan Technology Ltd. Poly(triaryl amine) (PTAA, 99.999% purity, Mwt: ~5,000–15,000) was supplied by Xi'an polymer. Formamidinium iodide (FAI, 99.99% purity), methylammonium bromide (MABr, 99.99% purity), and phenethylammonium iodide (PEAI, 98% purity) were received from GreatCell Solar Ltd. Lead (II) iodide (PbI_2, 99.999% purity) and lead (II) bromide ($PbBr_2$, 99.999% purity) were procured from Alfa Aesar. C_{60} (>99.5% purity) and bathocuproine (BCP, >99.5% purity) were purchased from Ossila Ltd. [2-(9H-Carbazol-9-yl)ethyl]phosphonic acid (2PACz, >98.0% purity) was purchased from TCI. PhenHCl (analytical standard), CsI (99.999% purity), dimethylformamide (DMF, anhydrous, ≥99.8% purity), dimethyl sulfoxide (DMSO, anhydrous, ≥99.9% purity), ethyl acetate (EtAc, anhydrous, 99.8% purity), chlorobenzene (CB, anhydrous, 99.8% purity), isopropanol (IPA, anhydrous, 99.5% purity), and silver (Ag shot, ≥99.99% purity) were purchased from Sigma-Aldrich. Copper pellets (Cu, 99.99% purity) were obtained from Kurt-J. Lesker company. All materials were used as received without further purification.

Solar cells fabrication

Fabrication and characterization of single-junction PSCs

The inverted (*p-i-n*) device stack consists of ITO-PTAA-$Cs_{0.15}MA_{0.15}FA_{0.70}Pb(I_{0.80}Br_{0.20})_3$-$C_{60}$-BCP-Ag. The devices were prepared using the following procedure. ITO glass substrates were cleaned by sonication successively in detergent, deionized water, acetone, and isopropanol. The sonication time was 15 min for each cleaning. They were then dried with N_2 flow and transferred to a glovebox filled with N_2. The hole transport layer, PTAA (2 mg/mL in CB), with a thickness of ~15 nm was spin coated on top of the ITO substrates at 6,000 rpm for 20 s and subsequently annealed at 100°C for 10 min. Prior to coating the perovskite layer, CsI (1.5 mg/mL in DMF) was spin coated onto the PTAA layer at 4,000 rpm for 40 s. Subsequent annealing of the film at 100°C for 5 min results in the formation of CsI islands on PTAA, which act as artificial nucleation sites. To coat the perovskite layer, the perovskite precursor solutions were prepared by dissolving CsI, FAI, MABr, PbI_2, and $PbBr_2$ salts in co-solvent of DMF/DMSO (4/1:v/v) to obtain 1.25 M of $Cs_{0.15}MA_{0.15}FA_{0.70}Pb(I_{0.80}Br_{0.20})_3$. The perovskite solutions were then coated onto the PTAA layer by using a consecutive two-step spin-coating process consisting of 2,000 rpm for 10 s and 5,000 rpm for 30 s. 300 μL of EtAc was dropped at the 10th second of the second step. The films were then annealed at 100°C for 25 min. For the GBP, certain concentrations of PhenHCl were added to the precursor solutions. On the other hand, to passivate the top surface of the perovskite layer, certain concentrations of PhenHCl dissolved in IPA were spin coated 4,000 rpm for 40 s followed by an annealing step. The devices were completed by thermal deposition of C_{60} (40 nm thick), BCP (8 nm thick), and Ag or Cu (100 nm thick) at a vacuum of $<3 \times 10^{-6}$ torr.

For the 2PACz-based devices, 2PACz solution with a concentration of 1 mg/mL in anhydrous ethanol was spin coated on the ITO layer at 3,000 rpm for 30 s. After spin coating, the substrates were heated at 100°C for 10 min. Unless stated otherwise, all of the *p-i-n* single-junction devices in this study were fabricated with PTAA HTL.

$Cs_{0.15}MA_{0.15}FA_{0.70}Pb(I_{0.80}Br_{0.20})_3$ perovskite thin films on ITO/PTAA stack with I-deficient (PbI_2-rich) surfaces were fabricated by overannealing the films at 100°C for 60 min.[44] On the other hand, to form Pb-deficient (MAI-rich) surfaces, the films were dipped in a solution of MAI (5 mg/mL in IPA) for 2 min at room temperature.[62] After these post-treatments, the I-deficient (PbI_2-rich) and Pb-deficient (MAI-rich) perovskite thin films were passivated with PhenHCl molecule using the optimized TSP recipe, and then, the devices were completed by thermal deposition of C_{60}, BCP, and Ag layers as described above.

Fabrication and characterization of perovskite/textured silicon tandem solar cells

Silicon heterojunction (SHJ) bottom cells were fabricated on float-zone double-side-textured four inches n-doped wafers with a resistivity of 1–5 Ω/cm and a thickness of 250–280 μm. The texturing process was done in an alkaline solution to get randomly distributed pyramids and cleaned in RCA1 and RCA2 solutions. The size of the pyramids was controlled by adjusting the alkaline concentration and the process temperature. The wafers were dipped in 5% hydrofluoric acid solution to remove the native oxide layer prior the PECVD depositions. The intrinsic, n, and p silicon amorphous layers were deposited in a PECVD cluster (Indeotec Octopus 2) with thicknesses of 8, 6, and 13 nm, respectively. The back electrode was deposited by sputtering sequentially ITO and Ag (150 and 250 nm, respectively) in the PVD part of the Octopus cluster. The ITO recombination junction (25 nm) was sputtered in an Angstrom EvoVac sputtering tool. The wafers are annealed at 200°C for 10 min to

recover the sputtering damage. 2PACz solution with a concentration of 1 mg/mL in anhydrous ethanol was spin coated on the ITO layer at 3,000 rpm for 30 s. After spin coating, the substrates were heated at 100°C for 10 min.[59] The perovskite layer was deposited using the single-junction device deposition recipe, except a 1.8 M of solution was spin coated on the textured surface. 150 μL of perovskite precursor solution was dropped on top of Si substrate and deposited by three consecutive spin-coating steps of 300, 1,500, and 5,000 rpm for 5, 90, and 10 s, respectively.[15] During the third spin-coating step (5,000 rpm), 300 μL solvent of ethyl acetate was quickly poured onto the substrate after 2 s. The perovskite-deposited films were annealed on a hotplate at 100°C for 20 min. 20 nm of C_{60} was thermally evaporated on top of the perovskite layer in an Angstrom EvoVac evaporation system. The SnO_x buffer layer (20 nm) was deposited by the thermal atomic layer deposition (ALD) technique using Picosun ALD cluster. Tetrakis(dimethylamino)tin and H_2O were used as precursors for the ALD deposition at 100°C and with 140 cycles. 100 nm of IZO top electrode (42 Ω/sq) was sputtered on the buffer layer in the Angstrom EvoVac sputtering system with RF power of 42 W over a 3-inch target (90% In_2O_3 / 10% ZnO, 99.9% Plasmaterials, the source to substrate distance is 10 cm). The top Ag contacts (250 nm) were evaporated through a shadow mask using an Angstrom EvoVac thermal evaporator with a rate of 2.5 Å/s. Finally, 140 nm of MgF_2 antireflection films were evaporated at a rate of 1 Å/s to complete the devices.

Device characterization

The single-junction devices (0.1 cm^2) were tested using a Keithley 2400 at room temperature under AM 1.5G illuminations (1,000 W/m^2) with an Abet Technologies Sun 3000 solar simulator, which was calibrated using a standard silicon cell (RERA). Current-voltage (*J-V*) curves were obtained both in reverse (1.2 → −0.1 V) and forward scan (−0.1 → 1.2 V) with a step size of 10 mV. All the measurements were performed under N_2 environment inside a glovebox. The tandem device *J-V* measurements were performed using Wavelabs Sinus 220 LED-based solar simulator with AM 1.5 G irradiance spectrum. The temperature was controlled during the measurement using a vacuum stage at 25°C. The illumination area of the devices was 1.03 cm^2, which was determined by the laser cut shadow mask coated with black paint. The EQE of the single-junction solar cells was measured with a commercial Newport EQE system under N_2 environment. The chopped monochromatic light beam was focused entirely on the active area of the solar cells. The tandem EQE measurements were performed using PV-Tools LOANA equipment. The tandem devices were light biased by IR LEDs (930 nm) when measuring the perovskite top cells, whereas the tandem devices were light biased by a blue LED when measuring the silicon bottom cells. MPP voltages were applied on the devices to enable the near short-circuit conditions for each sub-cells. The tandem EQE characterizations were performed at ambient air with RH ~50% and without any encapsulation. For transient photovoltage (TPV) measurements, a 405-nm laser diode was used to maintain solar cells at approximately V_{OC} conditions. Laser intensity was driven using an arbitrary waveform generator Agilent 33500B. A small perturbation was induced with a second 405-nm laser diode driven by a function generator from Agilent. The intensity of the short (50 ns) laser pulse was adjusted to keep the voltage perturbation below 10 mV, typically at 5 mV. Following the pulse, the voltage decays back to its steady-state value in a single exponential decay. The characteristic decay time was determined from a linear fit to a logarithmic plot of the voltage transient and returned the small perturbation charge carrier lifetime. Thermal admittance spectroscopy measurements were performed in a cryogenic probe station (Lakehore CRX-4K) under high vacuum (<10–^{5} mbar). Capacitance-frequency measurements were conducted in a frequency range of 1 MHz–10 Hz using a Solartron 1260A impedance

analyzer under dark equilibrium with 0 V forward bias and a perturbation signal with the modulation voltage of 20 mV. During the measurements, the sample temperature was varied from 320 to 250 K with 10 K steps. A delay time of 15 min was applied between the temperature values to obtain thermal stability.

Thin film characterization

A Cary 5000 UV-vis-NIR spectrophotometer was used to measure absorbance with PTAA-coated ITO glass substrates as references. The XRD patterns were recorded with a Bruker D2 Advance diffractometer (Bruker, PHASER) with Cu Kα radiation (λ = 1.5418 Å). The time-resolved PL (TRPL) measurements were conducted using a high-resolution streak camera system. The excitation beam at 532 nm (HELIOS 532-4-125, Coherent Inc.) with a pulse width of 0.85 ns and a repetition rate of 1 kHz was focused to excite the samples. The associated PL emission was collected by an optical telescope (consisting of two plano-convex lenses) and spectrally and temporally resolved using a spectrograph (PI Spectra Pro SP2300) and streak camera (Hamamatsu C10910) system with a temporal resolution of 1.4 ps. The data were acquired in photon counting mode using the streak camera software (HPDTA) and exported to Origin Pro for further analysis. After the deposition of perovskite layer on quartz substrates, the sample was placed in a sealed nitrogen chamber to prevent any changes due to exposure to oxygen and humidity. All measurements were done at room temperature. The steady-state PL spectra of the perovskite films coated on quartz were collected using FluoroMax (Horiba) system. The absolute PL spectra imaging of the samples were collected using IMA hyperspectral microscopy system (Photon, etc.). The sealed samples were excited at 532 nm (CW laser), and the excitation was set to 1-sun illumination. The absolute calibration procedure of the setup is reported in detail elsewhere.[75] Home-built MATLAB code was used for further investigation of QFLS, band gap, and Urbach energy. UPS and XPS measurements were conducted using an Omicron multi-probe photoemission spectroscopy (PES) system (base pressure of 3×10^{-10} mbar) equipped with a Sphera II EAC 125 hemispherical electron analyzer and a multi-channeltron electron detector. All measurements were carried out in electrical contact to the analyzer without charge neutralization. UPS was carried out at an electron escape angle of 90° with a focus HIS-13 helium discharge lamp with a He(1)α source (21.22 eV) 10–1 mbar He (90 mA, 570 V). A minor component (2.5%) of He(1)β 23.09 eV was deducted from the spectrum to identify the high KE valence band cutoff. A bias of −9.97 eV was applied to the sample. XPS was carried out at an electron escape angle of 57° with an Al Kα monochromated X-ray source (XM1000) at a power of 390 W. Calibration was made under the same experimental settings and conditions assigning the 0 binding energy position to Fermi level of an evaporated metallic Au reference sample in (UPS) and Fermi level and Au 4f7/2 difference (Δ84.2 eV). The photoelectron pass energy was fixed at 15 eV for high-resolution XPS, 50 eV survey XPS at 5 eV for the valence band region in UPS, and at 10 eV for the secondary electron cutoff SECO in UPS. Analysis of the perovskite substrate Pb4f and I3d core level peaks before and after surface deposition can be used to approximate the coverage of PhenHCl.[76,77]

DFT calculations

We used the Vienna *ab initio* simulation package,[78] the projector augmented wave method,[79] and the generalized gradient approximation of Perdew, Burke, and Ernzerhof. The cutoff energy was set to 450 eV, and the Brillouin zone was sampled on a Monkhorst-Pack 3 × 3 × 1 k-mesh. We augmented a 2 × 2 × 1 supercell of the tetragonal unit cell of $FAPbI_3$ along the *c*-axis with a vacuum slab of 20 Å thickness to create a PbI_2-terminated surface. A $Cs_{0.13}MA_{0.13}FA_{0.74}Pb(I_{0.81}Br_{0.19})_3$ composition was achieved by replacing four FA^+ molecules next to the PbI_2-terminated

surface with two MA^+ molecules and two Cs atoms as well as two I atoms in the PbI_2-terminated surface and seven I atoms in the next PbI_2-layer with Br atoms. The I-deficient surface was created by removing one I atom from the PbI_2-terminated surface, and the Pb-deficient surface was created by adding one I atom to a Pb-dangling bond. All structures were optimized until the total energy was converged to 10^{-5} eV, and the atomic forces were converged to 10^{-3} eV/Å. Bader charge analysis was carried out to analyze the charge transfer.[80] The binding energy was calculated as:

$$E[Cs_{0.13}MA_{0.13}FA_{0.74}Pb(I_{0.81}Br_{0.19})_3\text{-}PhenH^+/PEA^+] - E[Cs_{0.13}MA_{0.13}FA_{0.74}Pb(I_{0.81}Br_{0.19})_3] - E[PhenH^+/PEA^+],$$

where the three terms denote the total energies of $Cs_{0.13}MA_{0.13}FA_{0.74}Pb(I_{0.81}Br_{0.19})_3$ with molecule, $Cs_{0.13}MA_{0.13}FA_{0.74}Pb(I_{0.81}Br_{0.19})_3$ without molecule, and the molecule, respectively.

SUPPLEMENTAL INFORMATION

Supplemental information can be found online at https://doi.org/10.1016/j.joule.2021.05.013.

ACKNOWLEDGMENTS

The authors thank the members of the KAUST Solar Center operations team for their technical help and support. This publication is based upon work supported by the King Abdullah University of Science and Technology (KAUST) Office of Sponsored Research (OSR) under award no. KAUST OSR-2018-CARF/CCF-3079, OSR-2018-CPF-3669.02, KAUST OSR-CRG RF/1/3383, KAUST OSR-CRG2018-3737, and IED OSR-2019-4208.

AUTHOR CONTRIBUTIONS

Conceptualization, F.H.I.; methodology, F.H.I., F.F., and J.L.; validation, F.H.I., F.F., J.L., E.U., E.Y., M.K.E., A.S.S., M.D.B., G.T.H., S.Z., C.T.H., E.A., M.W., N.G., T.G.A., A.u.R., E.V.K., D.B., I.M., T.D.A., U.S., and S.D.W.; formal analysis, F.H.I., F.F., E.U., M.K.E., A.S.S., and M.D.B.; investigation, F.F., F.H.I., J.L., E.U., E.Y., M.K.E., G.T.H., S.Z., E.A., M.W., N.G., T.G.A., A.u.R., E.V.K., and D.B.; writing – original draft, F.H.I. and S.D.W.; visualization, F.H.I. and S.D.W.; supervision, F.H.I. and S.D.W.; writing – review & editing, A.S.S., M.D.B., G.T.H., D.B., I.M., T.D.A., and U.S.; project administration, S.D.W.; funding acquisition, S.D.W.

DECLARATION OF INTERESTS

The authors declare no competing interests.

Received: January 29, 2021
Revised: April 20, 2021
Accepted: May 14, 2021
Published: June 16, 2021

REFERENCES

1. National Renewable Energy Laboratory (2021). Best research-cell efficiencies. https://www.nrel.gov/pv/cell-efficiency.html.

2. De Wolf, S., Holovsky, J., Moon, S.J., Löper, P., Niesen, B., Ledinsky, M., Haug, F.J., Yum, J.H., and Ballif, C. (2014). Organometallic halide perovskites: sharp optical absorption edge and its relation to photovoltaic performance. J. Phys. Chem. Lett. *5*, 1035–1039.

3. Stranks, S.D., Eperon, G.E., Grancini, G., Menelaou, C., Alcocer, M.J., Leijtens, T., Herz, L.M., Petrozza, A., and Snaith, H.J. (2013). Electron-hole diffusion lengths exceeding 1 micrometer in an organometal trihalide perovskite absorber. Science *342*, 341–344.

4. Xing, G., Mathews, N., Sun, S., Lim, S.S., Lam, Y.M., Grätzel, M., Mhaisalkar, S., and Sum, T.C. (2013). Long-range balanced electron- and

hole-transport lengths in organic-inorganic CH3NH3PbI3. Science *342*, 344–347.

5. Li, F., Ma, C., Wang, H., Hu, W., Yu, W., Sheikh, A.D., and Wu, T. (2015). Ambipolar solution-processed hybrid perovskite phototransistors. Nat. Commun. *6*, 8238.

6. Ball, J.M., Lee, M.M., Hey, A., and Snaith, H.J. (2013). Low-temperature processed meso-superstructured to thin-film perovskite solar cells. Energy Environ. Sci. *6*, 1739–1743.

7. Yang, Y., Peng, H., Liu, C., Arain, Z., Ding, Y., Ma, S., Liu, X., Hayat, T., Alsaedi, A., and Dai, S. (2019). Bi-functional additive engineering for high-performance perovskite solar cells with reduced trap density. J. Mater. Chem. A *7*, 6450–6458.

8. Stoddard, R.J., Rajagopal, A., Palmer, R.L., Braly, I.L., Jen, A.K.-Y., and Hillhouse, H.W. (2018). Enhancing defect tolerance and phase stability of high-bandgap perovskites via guanidinium alloying. ACS Energy Lett *3*, 1261–1268.

9. Sutherland, B.R. (2020). Perovskite-silicon tandems edge forward. Joule *4*, 722–723.

10. Leijtens, T., Bush, K.A., Prasanna, R., and McGehee, M.D. (2018). Opportunities and challenges for tandem solar cells using metal halide perovskite semiconductors. Nat. Energy *3*, 828–838.

11. Aydin, E., Allen, T.G., De Bastiani, M., Xu, L., Ávila, J., Salvador, M., Van Kerschaver, E., and De Wolf, S. (2020). Interplay between temperature and bandgap energies on the outdoor performance of perovskite/silicon tandem solar cells. Nat. Energy *5*, 851–859.

12. Kim, D., Jung, H.J., Park, I.J., Larson, B.W., Dunfield, S.P., Xiao, C., Kim, J., Tong, J., Boonmongkolras, P., Ji, S.G., et al. (2020). Efficient, stable silicon tandem cells enabled by anion-engineered wide-bandgap perovskites. Science *368*, 155–160.

13. Subbiah, A.S., Isikgor, F.H., Howells, C.T., De Bastiani, M., Liu, J., Aydin, E., Furlan, F., Allen, T.G., Xu, F., Zhumagali, S., et al. (2020). High-performance perovskite single-junction and textured perovskite/silicon tandem solar cells via slot-die-coating. ACS Energy Lett *5*, 3034–3040.

14. Chen, B., Yu, Z.J., Manzoor, S., Wang, S., Weigand, W., Yu, Z., Yang, G., Ni, Z., Dai, X., Holman, Z.C., and Huang, J. (2020). Blade-coated perovskites on textured silicon for 26%-efficient monolithic perovskite/silicon tandem solar cells. Joule *4*, 850–864.

15. Hou, Y., Aydin, E., De Bastiani, M., Xiao, C., Isikgor, F.H., Xue, D.J., Chen, B., Chen, H., Bahrami, B., Chowdhury, A.H., et al. (2020). Efficient tandem solar cells with solution-processed perovskite on textured crystalline silicon. Science *367*, 1135–1140.

16. Huang, H.-H., Shih, Y.-C., Wang, L., and Lin, K.-F. (2019). Boosting the ultra-stable unencapsulated perovskite solar cells by using montmorillonite/CH3NH3PbI3 nanocomposite as photoactive layer. Energy Environ. Sci. *12*, 1265–1273.

17. Wang, R., Mujahid, M., Duan, Y., Wang, Z.-K., Xue, J., and Yang, Y. (2019). A review of perovskites solar cell stability. Adv. Funct. Mater. *29*, 1808843.

18. Ugur, E., Alarousu, E., Khan, J.I., Vlk, A., Aydin, E., De Bastiani, M., Balawi, A.H., Gonzalez Lopez, S.P., Ledinský, M., De Wolf, S., and Laquai, F. (2020). How humidity and light exposure change the photophysics of metal halide perovskite solar cells. Sol. RRL *4*, 2000382.

19. Ahn, N., Kwak, K., Jang, M.S., Yoon, H., Lee, B.Y., Lee, J.K., Pikhitsa, P.V., Byun, J., and Choi, M. (2016). Trapped charge-driven degradation of perovskite solar cells. Nat. Commun. *7*, 13422.

20. Domanski, K., Alharbi, E.A., Hagfeldt, A., Grätzel, M., and Tress, W. (2018). Systematic investigation of the impact of operation conditions on the degradation behaviour of perovskite solar cells. Nat. Energy *3*, 61–67.

21. Misra, R.K., Ciammaruchi, L., Aharon, S., Mogilyansky, D., Etgar, L., Visoly-Fisher, I., and Katz, E.A. (2016). Effect of halide composition on the photochemical stability of perovskite photovoltaic materials. ChemSusChem *9*, 2572–2577.

22. Hoke, E.T., Slotcavage, D.J., Dohner, E.R., Bowring, A.R., Karunadasa, H.I., and McGehee, M.D. (2015). Reversible photo-induced trap formation in mixed-halide hybrid perovskites for photovoltaics. Chem. Sci. *6*, 613–617.

23. Belisle, R.A., Bush, K.A., Bertoluzzi, L., Gold-Parker, A., Toney, M.F., and McGehee, M.D. (2018). Impact of surfaces on photoinduced halide segregation in mixed-halide perovskites. ACS Energy Lett *3*, 2694–2700.

24. Zhang, H., Fu, X., Tang, Y., Wang, H., Zhang, C., Yu, W.W., Wang, X., Zhang, Y., and Xiao, M. (2019). Phase segregation due to ion migration in all-inorganic mixed-halide perovskite nanocrystals. Nat. Commun. *10*, 1088.

25. Zhang, F., and Zhu, K. (2020). Additive engineering for efficient and stable perovskite solar cells. Adv. Energy Mater. *10*, 1902579.

26. Ball, J.M., and Petrozza, A. (2016). Defects in perovskite-halides and their effects in solar cells. Nat. Energy *1*, 16149.

27. Si, H., Xu, C., Ou, Y., Zhang, G., Fan, W., Xiong, Z., Kausar, A., Liao, Q., Zhang, Z., Sattar, A., et al. (2020). Dual-passivation of ionic defects for highly crystalline perovskite. Nano Energy *68*, 104320.

28. Liu, X., Yu, Z., Wang, T., Chiu, K.L., Lin, F., Gong, H., Ding, L., and Cheng, Y. (2020). Full defects passivation enables 21% efficiency perovskite solar cells operating in air. Adv. Energy Mater. *10*, 2001958.

29. Liu, X., Cheng, Y., Tang, B., Yu, Z.G., Li, M., Lin, F., Zhang, S., Zhang, Y.-W., Ouyang, J., and Gong, H. (2020). Shallow defects levels and extract detrapped charges to stabilize highly efficient and hysteresis-free perovskite photovoltaic devices. Nano Energy *71*, 104556.

30. Chen, B., Rudd, P.N., Yang, S., Yuan, Y., and Huang, J. (2019). Imperfections and their passivation in halide perovskite solar cells. Chem. Soc. Rev. *48*, 3842–3867.

31. Aydin, E., De Bastiani, M., and De Wolf, S. (2019). Defect and contact passivation for perovskite solar cells. Adv. Mater. *31*, e1900428.

32. Fu, L., Li, H., Wang, L., Yin, R., Li, B., and Yin, L. (2020). Defect passivation strategies in perovskites for an enhanced photovoltaic performance. Energy Environ. Sci. *13*, 4017–4056.

33. Maiti, A., Chatterjee, S., Peedikakkandy, L., and Pal, A.J. (2020). Defects and their passivation in hybrid halide perovskites toward solar cell applications. Sol. RRL *4*, 2000505.

34. Lee, J.-W., Bae, S.-H., Hsieh, Y.-T., De Marco, N., Wang, M., Sun, P., and Yang, Y. (2017). A bifunctional Lewis base additive for microscopic homogeneity in perovskite solar cells. Chem *3*, 290–302.

35. Ye, S., Rao, H., Zhao, Z., Zhang, L., Bao, H., Sun, W., Li, Y., Gu, F., Wang, J., Liu, Z., et al. (2017). A breakthrough efficiency of 19.9% obtained in inverted perovskite solar cells by using an efficient trap state passivator Cu(thiourea)I. J. Am. Chem. Soc. *139*, 7504–7512.

36. Zhang, F., Bi, D., Pellet, N., Xiao, C., Li, Z., Berry, J.J., Zakeeruddin, S.M., Zhu, K., and Grätzel, M. (2018). Suppressing defects through the synergistic effect of a Lewis base and a Lewis acid for highly efficient and stable perovskite solar cells. Energy Environ. Sci. *11*, 3480–3490.

37. Peng, J., Khan, J.I., Liu, W., Ugur, E., Duong, T., Wu, Y., Shen, H., Wang, K., Dang, H., Aydin, E., et al. (2018). A universal double-side passivation for high open-circuit voltage in perovskite solar cells: role of carbonyl groups in poly(methyl methacrylate). Adv. Energy Mater. *8*, 1801208.

38. Wang, R., Xue, J., Meng, L., Lee, J.-W., Zhao, Z., Sun, P., Cai, L., Huang, T., Wang, Z., Wang, Z.-K., et al. (2019). Caffeine improves the performance and thermal stability of perovskite solar cells. Joule *3*, 1464–1477.

39. Shao, S., Abdu-Aguye, M., Qiu, L., Lai, L.-H., Liu, J., Adjokatse, S., Jahani, F., Kamminga, M.E., ten Brink, G.H., Palstra, T.T.M., et al. (2016). Elimination of the light soaking effect and performance enhancement in perovskite solar cells using a fullerene derivative. Energy Environ. Sci. *9*, 2444–2452.

40. Islam, A., Li, J., Pervaiz, M., Lu, Z.-H., Sain, M., Chen, L., and Ouyang, X. (2019). Zwitterions for organic/perovskite solar cells, light-emitting devices, and lithium ion batteries: recent progress and perspectives. Adv. Energy Mater. *9*, 1803354.

41. Li, W., Lai, X., Meng, F., Li, G., Wang, K., Kyaw, A.K.K., and Sun, X.W. (2020). Efficient defect-passivation and charge-transfer with interfacial organophosphorus ligand modification for enhanced performance of perovskite solar cells. Sol. Energy Mater. Sol. Cells *211*, 110527.

42. Yang, Z., Feng, W., Yu, C., Jian-Pu, W., Hong-Hua, F., Antonietta, L.M., Ni, Z., and Ching-Ping, W. (2017). Benzylamine-treated wide-bandgap perovskite with high thermal-photostability and photovoltaic performance. Adv. Energy Mater. *7*, 1701048.

43. Wang, F., Geng, W., Zhou, Y., Fang, H.H., Tong, C.J., Loi, M.A., Liu, L.M., and Zhao, N. (2016). Phenylalkylamine passivation of organolead halide perovskites enabling high-

efficiency and air-stable photovoltaic cells. Adv. Mater. *28*, 9986–9992.

44. Wu, W.Q., Rudd, P.N., Ni, Z., Van Brackle, C.H., Wei, H., Wang, Q., Ecker, B.R., Gao, Y., and Huang, J. (2020). Reducing surface halide deficiency for efficient and stable iodide-based perovskite solar cells. J. Am. Chem. Soc. *142*, 3989–3996.

45. Bert, C., Jeroen, D., Nicolas, G., Aslihan, B., Jan, D.H., Lien, D.O., Anitha, E., Jo, V., Jean, M., Edoardo, M., et al. (2015). Intrinsic thermal instability of methylammonium lead trihalide perovskite. Adv. Energy Mater. *5*, 1500477.

46. Ma, L., Guo, D., Li, M., Wang, C., Zhou, Z., Zhao, X., Zhang, F., Ao, Z., and Nie, Z. (2019). Temperature-dependent thermal decomposition pathway of organic–inorganic halide perovskite materials. Chem. Mater. *31*, 8515–8522.

47. Li, M.H., Yeh, H.H., Chiang, Y.H., Jeng, U.S., Su, C.J., Shiu, H.W., Hsu, Y.J., Kosugi, N., Ohigashi, T., Chen, Y.A., and Guo, T.F. (2018). Highly efficient 2D/3D hybrid perovskite solar cells via low-pressure vapor-assisted solution process. Adv. Mater. *30*, e1801401.

48. Ke, W., Mao, L., Stoumpos, C.C., Hoffman, J., Spanopoulos, I., Mohite, A.D., and Kanatzidis, M.G. (2019). Compositional and solvent engineering in Dion–Jacobson 2D perovskites boosts solar cell efficiency and stability. Adv. Energy Mater. *9*, 1803384.

49. Wang, Z., Lin, Q., Chmiel, F.P., Sakai, N., Herz, L.M., and Snaith, H.J. (2017). Efficient ambient-air-stable solar cells with 2D–3D heterostructured butylammonium-caesium-formamidinium lead halide perovskites. Nat. Energy *2*, 17135.

50. Gharibzadeh, S., Abdollahi Nejand, B., Jakoby, M., Abzieher, T., Hauschild, D., Moghadamzadeh, S., Schwenzer, J.A., Brenner, P., Schmager, R., Haghighirad, A.A., et al. (2019). Record open-circuit voltage wide-bandgap perovskite solar cells utilizing 2D/3D perovskite heterostructure. Adv. Energy Mater. *9*, 1803699.

51. De Bastiani, M., Subbiah, A.S., Aydin, E., Isikgor, F.H., Allen, T.G., and De Wolf, S. (2020). Recombination junctions for efficient monolithic perovskite-based tandem solar cells: physical principles, properties, processing and prospects. Mater. Horiz. *7*, 2791–2809.

52. Zheng, X., Deng, Y., Chen, B., Wei, H., Xiao, X., Fang, Y., Lin, Y., Yu, Z., Liu, Y., Wang, Q., and Huang, J. (2018). Dual functions of crystallization control and defect passivation enabled by sulfonic zwitterions for stable and efficient perovskite solar cells. Adv. Mater. *30*, e1803428.

53. Xue, J., Wang, R., and Yang, Y. (2020). The surface of halide perovskites from nano to bulk. Nat. Rev. Mater. *5*, 809–827.

54. Jiang, Q., Zhao, Y., Zhang, X., Yang, X., Chen, Y., Chu, Z., Ye, Q., Li, X., Yin, Z., and You, J. (2019). Surface passivation of perovskite film for efficient solar cells. Nat. Photonics *13*, 460–466.

55. Hu, Y., Schlipf, J., Wussler, M., Petrus, M.L., Jaegermann, W., Bein, T., Müller-Buschbaum, P., and Docampo, P. (2016). Hybrid perovskite/perovskite heterojunction solar cells. ACS Nano *10*, 5999–6007.

56. Jung, M., Shin, T.J., Seo, J., Kim, G., and Seok, S.I. (2018). Structural features and their functions in surfactant-armoured methylammonium lead iodide perovskites for highly efficient and stable solar cells. Energy Environ. Sci. *11*, 2188–2197.

57. Rajagopal, A., Stoddard, R.J., Jo, S.B., Hillhouse, H.W., and Jen, A.K.Y. (2018). Overcoming the photovoltage plateau in large bandgap perovskite photovoltaics. Nano Lett *18*, 3985–3993.

58. Wang, H., Zhu, C., Liu, L., Ma, S., Liu, P., Wu, J., Shi, C., Du, Q., Hao, Y., Xiang, S., et al. (2019). Interfacial residual stress relaxation in perovskite solar cells with improved stability. Adv. Mater. *31*, e1904408.

59. Al-Ashouri, A., Magomedov, A., Roß, M., Jošt, M., Talaikis, M., Chistiakova, G., Bertram, T., Márquez, J.A., Köhnen, E., Kasparavičius, E., et al. (2019). Conformal monolayer contacts with lossless interfaces for perovskite single junction and monolithic tandem solar cells. Energy Environ. Sci. *12*, 3356–3369.

60. Rühle, S. (2016). Tabulated values of the Shockley-Queisser limit for single junction solar cells. Sol. Energy *130*, 139–147.

61. Stolterfoht, M., Caprioglio, P., Wolff, C.M., Márquez, J.A., Nordmann, J., Zhang, S., Rothhardt, D., Hörmann, U., Amir, Y., Redinger, A., et al. (2019). The impact of energy alignment and interfacial recombination on the internal and external open-circuit voltage of perovskite solar cells. Energy Environ. Sci. *12*, 2778–2788.

62. Burschka, J., Pellet, N., Moon, S.J., Humphry-Baker, R., Gao, P., Nazeeruddin, M.K., and Grätzel, M. (2013). Sequential deposition as a route to high-performance perovskite-sensitized solar cells. Nature *499*, 316–319.

63. Isikgor, F.H., Li, B., Zhu, H., Xu, Q., and Ouyang, J. (2016). High performance planar perovskite solar cells with a perovskite of mixed organic cations and mixed halides, MA1-xFAxPbI3-yCly. J. Mater. Chem. A *4*, 12543–12553.

64. Jeon, N.J., Noh, J.H., Kim, Y.C., Yang, W.S., Ryu, S., and Seok, S.I. (2014). Solvent engineering for high-performance inorganic–organic hybrid perovskite solar cells. Nat. Mater. *13*, 897–903.

65. Calado, P., Telford, A.M., Bryant, D., Li, X., Nelson, J., O'Regan, B.C., and Barnes, P.R.F. (2016). Evidence for ion migration in hybrid perovskite solar cells with minimal hysteresis. Nat. Commun. *7*, 13831.

66. Knight, A.J., and Herz, L.M. (2020). Preventing phase segregation in mixed-halide perovskites: a perspective. Energy Environ. Sci. *13*, 2024–2046.

67. Abdi-Jalebi, M., Andaji-Garmaroudi, Z., Cacovich, S., Stavrakas, C., Philippe, B., Richter, J.M., Alsari, M., Booker, E.P., Hutter, E.M., Pearson, A.J., et al. (2018). Maximizing and stabilizing luminescence from halide perovskites with potassium passivation. Nature *555*, 497–501.

68. Braly, I.L., deQuilettes, D.W., Pazos-Outón, L.M., Burke, S., Ziffer, M.E., Ginger, D.S., and Hillhouse, H.W. (2018). Hybrid perovskite films approaching the radiative limit with over 90% photoluminescence quantum efficiency. Nat. Photonics *12*, 355–361.

69. El-Hajje, G., Momblona, C., Gil-Escrig, L., Ávila, J., Guillemot, T., Guillemoles, J.-F., Sessolo, M., Bolink, H.J., and Lombez, L. (2016). Quantification of spatial inhomogeneity in perovskite solar cells by hyperspectral luminescence imaging. Energy Environ. Sci. *9*, 2286–2294.

70. Stolterfoht, M., Wolff, C.M., Márquez, J.A., Zhang, S., Hages, C.J., Rothhardt, D., Albrecht, S., Burn, P.L., Meredith, P., Unold, T., and Neher, D. (2018). Visualization and suppression of interfacial recombination for high-efficiency large-area pin perovskite solar cells. Nat. Energy *3*, 847–854.

71. Yoon, S.J., Kuno, M., and Kamat, P.V. (2017). Shift happens. How halide ion defects influence photoinduced segregation in mixed halide perovskites. ACS Energy Lett *2*, 1507–1514.

72. Xu, J., Boyd, C.C., Yu, Z.J., Palmstrom, A.F., Witter, D.J., Larson, B.W., France, R.M., Werner, J., Harvey, S.P., Wolf, E.J., et al. (2020). Triple-halide wide–band gap perovskites with suppressed phase segregation for efficient tandems. Science *367*, 1097–1104.

73. Lv, B., Qian, T., and Ding, H. (2019). Angle-resolved photoemission spectroscopy and its application to topological materials. Nat. Rev. Phys. *1*, 609–626.

74. Al-Ashouri, A., Köhnen, E., Li, B., Magomedov, A., Hempel, H., Caprioglio, P., Márquez, J.A., Morales Vilches, A.B., Kasparavicius, E., Smith, J.A., et al. (2020). Monolithic perovskite/silicon tandem solar cell with >29% efficiency by enhanced hole extraction. Science *370*, 1300–1309.

75. Delamarre, A., Lombez, L., and Guillemoles, J.-F. (2012). Characterization of solar cells using electroluminescence and photoluminescence hyperspectral images. J. Photonics Energy *2*, 027004.

76. Wilson, J.N., Dowler, R.M., and Idriss, H. (2011). Adsorption and reaction of glycine on the rutile TiO2(011) single crystal surface. Surf. Sci. *605*, 206–213.

77. Seah, M.P. (2012). Simple universal curve for the energy-dependent electron attenuation length for all materials. Surf. Interface Anal. *44*, 1353–1359.

78. Kresse, G., and Joubert, D. (1999). From ultrasoft pseudopotentials to the projector augmented-wave method. Phys. Rev. B *59*, 1758–1775.

79. Blöchl, P.E. (1994). Projector augmented-wave method. Phys. Rev. B Condens. Matter *50*, 17953–17979.

80. Tang, W., Sanville, E., and Henkelman, G. (2009). A grid-based Bader analysis algorithm without lattice bias. J. Phys. Condens. Matter *21*, 084204.